



# 1 **Alicenet - An Italian network of Automated Lidar-Ceilometers for** 2 **4D aerosol monitoring: infrastructure, data processing, and** 3 **applications**

4 Annachiara Bellini<sup>1,2,3,\*</sup>, Henri Diémoz<sup>3</sup>, Luca Di Liberto<sup>2</sup>, Gian Paolo Gobbi<sup>2</sup>, Alessandro Bracci<sup>4</sup>,  
5 Ferdinando Pasqualini<sup>4</sup>, Francesca Barnaba<sup>2,\*</sup>

6 <sup>1</sup> University 'La Sapienza', DIET, Rome, Italy

7 <sup>2</sup> National Research Council - Institute of Atmospheric Science and Climate, CNR-ISAC, Rome, Italy

8 <sup>3</sup> ARPA Valle d'Aosta, Saint-Christophe, Italy

9 <sup>4</sup> National Research Council - Institute of Atmospheric Science and Climate, CNR-ISAC, Bologna, Italy

10 **\*Correspondence:** Francesca Barnaba ([f.barnaba@isac.cnr.it](mailto:f.barnaba@isac.cnr.it)) and Annachiara Bellini ([a.bellini@arpa.vda.it](mailto:a.bellini@arpa.vda.it))

11 **Abstract.** The vertically-resolved information on aerosol particles represents a key aspect in many atmospheric studies,  
12 ranging from aerosol-climate interactions to those investigating aerosol impacts on air quality and human health. This kind  
13 of information can be primarily derived by lidar active remote sensing and extended networks of these systems are currently  
14 run at the global scale. A network of Automated Lidar-Ceilometers (ALCs), Alicenet, was set up in Italy in 2015 by the  
15 Institute of Atmospheric Sciences and Climate (ISAC) of the National Research Council (CNR). Alicenet grew up in these  
16 years as a cooperative effort of Italian institutions dealing with atmospheric science and monitoring, and includes regional  
17 Environmental Protection Agencies, Universities and Research Centres. In the current configuration, the network runs both  
18 single-channel ALCs and dual channel, polarisation-sensitive systems (PLCs) operating in very different environments  
19 (urban, coastal, mountainous and volcanic areas) from Northern to Southern Italy, thus allowing the continuous monitoring  
20 of the aerosol vertical distribution across the country. Alicenet also contributes to the EUMETSAT program E-PROFILE,  
21 filling an Italian observational gap compared to other EU Member States. In this work, we present the Alicenet infrastructure  
22 and a detailed description of the specifically-developed data processing chain converting raw instrumental (Level 0) data into  
23 quantitative information on aerosol properties, with output products ranging from attenuated backscatter to aerosol mass and  
24 vertical stratification from the surface up to the upper troposphere (output data Levels 1-3). Overall, this setup provides from  
25 near real-time to long-term overviews of the 4D aerosol field over Italy. Examples of both are reported in this work. Specific  
26 comparisons of the Alicenet products to relevant independent measurements of different parameters (e.g. surface PM<sub>10</sub>,  
27 sunphotometer AOD) are also included, revealing the good performances of the Alicenet algorithms. Overall, Alicenet  
28 represents a valuable resource to extend the current aerosol observational capabilities in Italy and in the Central European  
29 Mediterranean area, and contributes to bridge a gap between atmospheric science and its application to specific sectors,  
30 among which: a) air quality, b) solar energy, c) aviation safety. More in general, the maturity of the ALC/PLC



31 instrumentation and of the data processing tools available within the wider international scientific/technical atmospheric  
32 community suggest lidar-ceilometer networks could usefully integrate current EU Atmospheric Research Infrastructures for  
33 aerosol studies.

## 34 **1. Introduction**

35 Aerosols influence the Earth radiation budget directly by extinction of solar radiation and indirectly by modification of cloud  
36 properties and lifetime, thus also influencing the hydrological cycle (IPCC, 2022). Atmospheric particles of both  
37 anthropogenic and natural origin are also a main concern for human health worldwide (WHO, 2021). High aerosol loads also  
38 reduce visibility and, particularly during major events (e.g. desert dust storms, volcanic eruptions, wide forest fires), could  
39 represent a threat for the transport sector, and particularly for aviation (e.g. Flentje et al., 2010; Papagiannopoulos et al,  
40 2020, Brenot et al., 2021; Monteiro et al., 2022). A key aspect to correctly quantify aerosol impacts on climate and society is  
41 represented by the aerosol vertical distribution. In fact, it affects radiative transfer balance and atmospheric heating rate (e.g.,  
42 Fasano et al., 2021; Fountoulakis et al. 2022), aerosol-cloud-precipitation interactions (e.g., Napoli et al., 2022), and large-  
43 to-small scale atmospheric processes influencing local air quality (e.g., Curci et al., 2015; Gobbi et al., 2019; Diémoz et al.,  
44 2019a,b) and high-elevation environments (Balestrini et al., 2024).

45 Active remote sensing through lidar sensors is a very efficient tool to provide range-resolved, accurate profiles of aerosol  
46 properties (e.g., Gobbi et al., 2001; Tesche et al. 2009; Ansmann et al., 2011). In the last decades, both ground-based and  
47 space-based lidar systems have been developed and widely used for scientific research purposes, and they are expected to  
48 play an increasingly important role in climate studies and public health (Remer et al., 2024). From space, the recently  
49 dismissed NASA-CNES CALIPSO sensor (Winker et al., 2010) provided one of the most valuable, vertically-resolved,  
50 global aerosol datasets (2006-2023), that is expected to be extended by the upcoming ESA mission EarthCARE (Cloud,  
51 Aerosol and Radiation Explorer, Illingworth et al., 2015). From the ground, lidar remote sensing is often performed in the  
52 framework of globally distributed research networks. In Europe, a wide Aerosol Research Lidar Network (EARLINET,  
53 Pappalardo et al., 2010) has been developed in the last decade, which is currently an important component of the European  
54 Strategy Forum on Research Infrastructures (ESFRI) ACTRIS. Such a research-oriented network runs high power, multi-  
55 wavelength Raman lidar systems, which were not designed for monitoring purposes. In fact, ACTRIS lidar measurements  
56 are generally not performed continuously, and the spatial density of the measuring sites (about 30 active systems covering  
57 Europe) is still insufficient to capture the high spatial and temporal variability characterising aerosols. These high-power  
58 systems are also affected by a thick blind region in the lowermost atmospheric levels, which strongly limits their utility in  
59 monitoring boundary layer processes. Only recently, ACTRIS started considering using automatic low-power lidars  
60 (hereafter referred to as Automated Lidar-Ceilometers, ALCs) as useful tools within its aerosol remote sensing (ARS)  
61 component, although these systems are not yet included in the relevant 'minimum' or 'optimal' setups recommended by  
62 ACTRIS-ARS (<https://www.actris.eu/topical-centre/cars/announcements-resources/documents>, last access 7 March 2024),  
63 and are rather only included within the ACTRIS-Cloud remote sensing component for liquid-cloud detection.



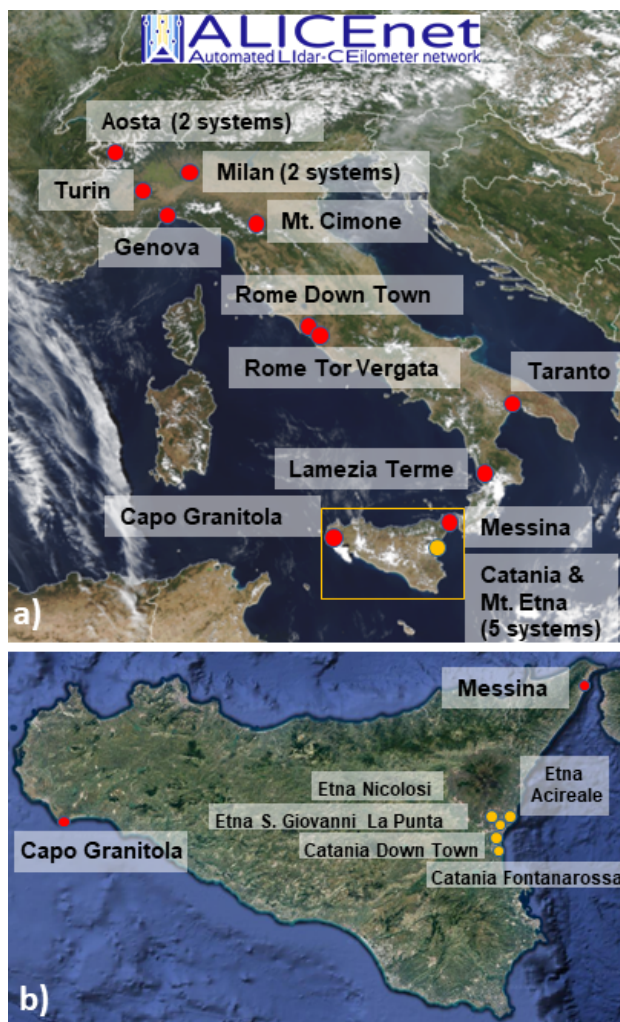
64 In fact, in the last two decades, technological improvements allowed the development of low-energy, eye safe, affordable  
65 and robust single-channel ALCs, originally conceived to only monitor the ‘cloud ceiling’. These systems emit single-  
66 wavelength laser pulses, mostly in the infrared range and, similarly to high power lidars, measure the time- (thus range-)  
67 dependent radiation elastically scattered back to the instrument by atmospheric components (molecules, aerosols, cloud  
68 droplets/ice crystals). Although with a lower signal-to-noise (SNR) ratio with respect to their high-power counterpart, a  
69 major advantage of ALCs is their ability to operate continuously, reliably and unattended, providing continuous information  
70 on aerosol profiles and clouds within the troposphere in near-real time. This favoured the development of extended ALC  
71 networks worldwide. These include the NASA Micro-Pulse Lidar Network (MPLnet; Welton et al., 2018), the US  
72 Environmental Protection Agency (EPA) network for Photochemical Assessment Monitoring Stations (PAMS; Caicedo et  
73 al., 2020), or the Asian Dust and aerosol lidar observation network (ADnet; Shimizu et al., 2016). In Europe, several  
74 Member States currently run dense ALC networks for monitoring purposes, mostly managed by National Meteo Services  
75 (e.g., the DWD in Germany or the MetOffice in the UK; Flentje et al., 2021; Osborne et al., 2022). In Europe, most of such  
76 ALC observations are also collected and further exploited in the framework of the E-PROFILE program run by the European  
77 Meteorological Services Network EUMETNET ([http://www.eumetnet.eu/activities/observations-programme/current-  
78 activities/e-profile/](http://www.eumetnet.eu/activities/observations-programme/current-activities/e-profile/), last access: 06-03-2024). The development of such an extended ALC observational capacity was very  
79 useful, for example, during the eruption of the Icelandic volcano Eyjafjallajökull in 2010, during which a readily accessible  
80 information on the aerosol plume horizontal and vertical displacement was needed, considering the major impact on aerial  
81 transport (Flentje et al., 2010, Mortier et al., 2013). More in general, ALC data can be used to study a variety of atmospheric  
82 processes related to aerosols, fog (Haeffelin et al., 2016), and clouds (Van Tricht et al., 2014), with benefits for a range of  
83 users in several socio-economic sectors. In particular, ALCs have been proven to be extremely useful in support of surface  
84 Air Quality (AQ) evaluations. In fact, they can provide information on the vertical dilution of pollutants, and are able to  
85 detect transboundary transport of particles from medium-to-long-range distances (e.g., Bucci et al., 2018; Diémoz et al.,  
86 2019a,b), secondary aerosol layers forming aloft, or even particles reaching down to the boundary layer through evaporating  
87 rain (virgas, e.g., Karle et al., 2023). However, with few exceptions, standard Air Quality Monitoring Networks (AQMNs)  
88 currently miss such profiling capability. The feasibility of filling this gap is currently explored in the framework of the EC-  
89 H2020 Project RI-URBANS (<https://riurbans.eu>, last access: 7 March 2024), aiming at the development of service tools in  
90 support to urban AQ monitoring in European urban centres and pollution hotspots. In fact, the current ALC technology has  
91 been proven to be mature enough to allow a robust retrieval of the planetary boundary layer height (Kotthaus et al., 2023), a  
92 key parameter in AQ, and evaluations are currently ongoing at the EU level to assess readiness of ALC-based retrievals for  
93 quantitative Particulate Matter (PM) monitoring (e.g., Shang et al., 2021). This is done for example in the framework of the  
94 EU Action PROBE (PROfiling the atmospheric Boundary layer at European scale; Cimini et al., 2020) supported by the  
95 European Cooperation in Science and Technology (COST), as well as within the E-PROFILE and ACTRIS communities.  
96 In Italy, an effort to coordinate ALCs activity at national level has been done by the National Research Council -Institute of  
97 Atmospheric Sciences and Climate of the (CNR-ISAC), which set up the Alicenet network in 2015 ([5  
6](https://www.alice-</a></p></div><div data-bbox=)



98 [net.eu/](https://net.eu/), last access: 7 March 2024) and is currently contributing to E-PROFILE, filling an observational gap over Italy, if  
99 compared to other EU Member States. These observations are particularly relevant for the Mediterranean area, this being a  
100 climatic hotspot (IPCC, 2022) and a crossroad of large scale fluxes from Continental Europe, North America, Africa and  
101 Asia (Lelieveld et al., 2002). In this area, the atmospheric circulation also features a wide spectrum of mesoscale fluxes  
102 triggered by complex topography. The resulting aerosol mixture is also a complex cocktail of anthropogenic, marine, desert  
103 dust, and biomass burning particles (e.g., Barnaba and Gobbi, 2004; Di Iorio et al., 2009, Andres Hernandez et al., 2022).  
104 The present work aims at presenting the Alicenet infrastructure and its data processing chain, specifically designed to derive  
105 quantitative information on vertically-resolved aerosol properties and layering. Alicenet is an open consortium coordinated  
106 by CNR-ISAC with contributions from several collaborating Partners (regional Environmental Protection Agencies,  
107 Universities, Research Institutions, and private companies). The ALC data processing is centralised at CNR-ISAC, allowing  
108 the retrieval of homogeneous quantitative ALC-based aerosol information from North to South Italy. The Alicenet  
109 processing chain is based on specifically developed retrieval algorithms, taking benefit from past and ongoing collaborations  
110 with the EU ALC-community, and particularly in the framework of the EU COST Actions TOPROF (2013-2016) and  
111 PROBE (2019-2024), the H2020 Project RI-URBANS, and the E-PROFILE initiative.  
112 The work is organised as follows: Sect 2 describes the Alicenet infrastructure. Sect. 3 introduces the data processing and  
113 includes specific examples of the Alicenet-based products further compared to independent datasets. In Sect. 4, three recent  
114 examples of the near-real time Alicenet monitoring capability are reported. A final summary is given in Sect. 5, this also  
115 describing some foreseen future developments.

## 116 2. Alicenet sites and instruments

117 The Alicenet stations are geographically distributed from the North to the South of the Italian peninsula as shown in Fig. 1.  
118 The network configuration also allows the monitoring of aerosol vertical profiles over a wide range of environmental and  
119 atmospheric conditions (e.g. urban, coastal and mountain) within the Mediterranean area. In fact, some sites are located in  
120 highly anthropized areas, such as those in the Po Valley and main urban/industrial sites in Italy (Milan, Genova, Turin,  
121 Rome, Taranto). Most sites are frequently impacted by desert dust advections, particularly relevant in Central and Southern  
122 Italy (e.g. Barnaba et al., 2017; Gobbi et al., 2019; Barnaba et al., 2022), and vegetation fires (e.g. Barnaba et al., 2011).  
123 Episodes of volcanic plumes transport are also registered in the Alicenet southernmost sites, mostly in the 5 stations located  
124 at the foothills of the Etna volcano, and in the Messina and Lamezia Terme stations, due to their proximity to the other active  
125 Sicilian volcano of Stromboli.



127 **Figure 1:** Location of the Alicenet stations (panel a, bullets). The yellow rectangle over Sicily in panel a) is zoomed in panel b) to show  
128 location of the 5 stations in the area extending from the Etna volcano southern foothills to the city of Catania. Maps: a) satellite true colour  
129 image (credits: EUMETSAT), and b) credits: © Google Maps.

130

131 For homogeneity of operations, since the beginning of the Alicenet activities (1<sup>st</sup> January 2016), it was agreed to operate  
132 standardised systems across the network choosing the ones having a sufficiently high SNR. The single-channel CHM15k  
133 instruments manufactured by Lufft (formerly Ott Hydromet) were selected for this purpose. These are bi-static ALCs with a  
134 Nd : YAG solid-state laser emitting linearly polarised light at 1064 nm, with a 5-7 kHz repetition rate, a maximum vertical  
135 resolution of 5 m and a maximum range of 15 km. The only exception in this instrumental setup was a modified-CHM15K  
136 prototype with polarisation-sensitive capabilities developed in 2013 by Jenoptik ESW in the framework of the EC Life+



137 DIAPASON project (Gobbi et al., 2019). This first ever polarisation-sensitive ALC (hereafter PLC) was intended to explore  
 138 the possibility to produce an affordable, robust system to be widely used in the identification and profiling of non-spherical  
 139 (e.g. mineral dust) aerosol layers. The prototype PLC was tested in Rome (Italy), where it has been operating successfully  
 140 since then (e.g., Gobbi et al., 2019; Andres Hernandez et al., 2022), but was never marketed by Lufft. More recently, PLC  
 141 systems have been made available on the market by Vaisala (CL61 systems, operating at 910 nm) and, due to the important  
 142 capability of such instruments to discriminate particle sphericity/non sphericity, these are being progressively included in  
 143 Alicenet.  
 144 For both CHM15k ALCs and CL61 PLCs, the signal is characterised by high temporal and vertical resolution, with some  
 145 variability depending on the system type and configuration (e.g., in Alicenet the CHM15k standard configuration implies a  
 146 vertical (temporal) resolution of 15 m (15 s)). A summary table with details on the Alicenet sites and instrumentation  
 147 operating therein is provided in Table 1.  
 148

Name	Lat	Lon	Altitude (m asl)	System Type	Reference Institution (& Collaborating Institution)
Aosta 1	45° 44' 32" N	07° 21' 24" E	555	ALC (Lufft CHM15K)	Arpa Valle d'Aosta (CNR-ISAC)
Aosta 2	45° 44' 32" N	07° 21' 24" E	555	PLC (Vaisala CL61)	Arpa Valle d'Aosta (CNR-ISAC)
Milano Bicocca	45° 30' 38" N	09° 12' 42" E	135	ALC (Lufft CHM15K)	CNR-ISAC (Univ. Milano Bicocca)
Milano Rubattino	45° 28' 38" N	09° 15' 41" E	110	PLC (Vaisala CL61)	RSE (CNR-ISAC)
Torino	45° 03' 28" N	7° 39' 24" E	250	PLC (Vaisala CL61)	Politecnico Torino (CNR-ISAC)
Genova	44° 24' 41" N	08° 53' 3" E	10	PLC (Vaisala CL61)	Arpa Liguria (CNR-ISAC)
Monte Cimone	44° 11' 35" N	10° 42' 05" E	2165	ALC (Lufft CHM15K)	CNR-ISAC





Rome Down Town	41° 54' 34" N	12° 29' 48" E	58	PLC (Lufft Prototype)	CNR-ISAC (Arpa Lazio)
Rome Tor Vergata	41° 50' 32" N	12° 38' 50" E	100	ALC (Lufft CHM15K)	CNR-ISAC
Taranto	40° 29' 37" N	17° 13' 01" E	17	ALC (Lufft CHM15K)	Arpa Puglia (CNR-ISAC)
Lamezia Terme	38° 52' 35" N	16° 13' 56"	5	ALC (Lufft CHM15K)	CNR-ISAC
Messina	38° 11' 41" N	15° 34' 22" E	5	ALC (Lufft CHM15K)	CNR-ISAC (CNR-IRBIM)
Etna Acireale	37° 38' 26" N	15° 10' 55" E	12	ALC (Lufft CHM15K)	Etna High Tech (CNR-ISAC, INGV)
Etna Nicolosi	37° 36' 49" N	15° 01' 11" E	730	PLC (Vaisala CL61)	INGV (CNR-ISAC, Etna High Tech)
Etna San Giovanni La Punta	37° 34' 44" N	15° 06' 11" E	350	ALC (Lufft CHM15K)	Etna High Tech (CNR-ISAC, INGV)
Capo Granitola	37° 34' 16" N	12° 39' 35" E	5	ALC (Lufft CHM15K)	CNR-ISAC
Catania Down Town	37° 30' 49" N	15° 04' 55" E	40	ALC (Lufft CHM15K)	INGV (CNR-ISAC, Etna High Tech)
Catania Fontanarossa	37° 27' 59" N	15° 04' 57" E	10	ALC (Lufft CHM15K)	SAC (Etna High Tech, CNR-ISAC, INGV)

**Table 1:** Alicenet sites from northern to southern Italy, and relevant details.

149

150

151

152

13

14



### 153 3. Alicenet data processing and relevant products

154 As in any backscatter lidar, the raw signal recorded by the ALCs is a function of the distance from the emitter (range,  $r$ ) and  
155 the emission/reception time  $t$ , and can be described through the lidar equation:

$$156 \quad P(r, t) = r^{-2} \text{Ovl}(r, t) C_L(t) (\beta_p(r, t) + \beta_m(r, t)) e^{-2 \int_0^r (\alpha_p(r', t) + \alpha_m(r', t)) dr'} \quad (1)$$

157 Equation 1 includes the particles (p) and molecules (m) backscatter ( $\beta$ ) and extinction ( $\alpha$ ) coefficients at the laser wavelength  
158 (elastic scattering), and some instrumental factors, embedded into the instrument-specific calibration coefficient  $C_L(t)$ .  
159 Furthermore, particularly for bistatic systems (i.e., the CHM15k), measurements in the near range are generally affected by  
160 signal losses due to the incomplete superposition (overlap) of the laser beam and the receiver field of view, this depending  
161 on the range and the time-varying instrument characteristics. The term  $\text{Ovl}(r, t)$  in Eq. 1 therefore indicates an instrument-  
162 specific overlap function used to quantify the signal loss in the near range. The total attenuated backscatter,  $\beta_{\text{att}}$ , i.e., the total  
163 (aerosol + molecules) backscatter coefficients attenuated by the total (aerosol + molecular) atmospheric transmission, can be  
164 simply derived from Eq. 1 as:

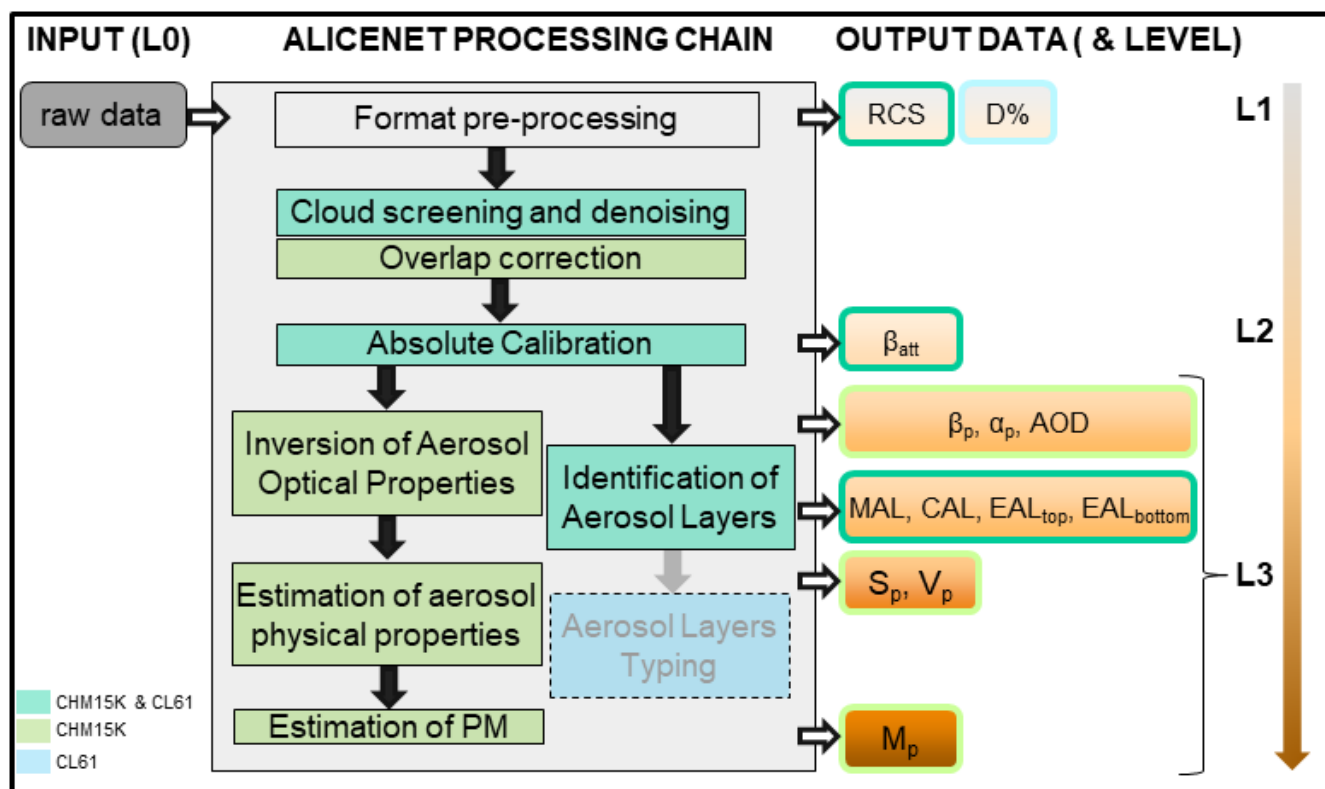
$$165 \quad \beta_{\text{att}}(r, t) = \frac{P(r, t) r^2}{\text{Ovl}(r, t) C_L(t)} = (\beta_p(r, t) + \beta_m(r, t)) e^{-2 \int_0^r (\alpha_p(r', t) + \alpha_m(r', t)) dr'} \quad (2)$$

166 In this section, the Alicenet data processing chain and main inputs and outputs (Fig. 2) are described. Each step of the  
167 processing chain is functional to derive specific terms of Eq. 1, and finally retrieve quantitative aerosol information from the  
168 ALC raw data. The procedure takes as input the ALC data formatted through the E-PROFILE Raw2L1 routine (main  
169 variables are the range-corrected signal,  $\text{RCS}(r, t) = P(r, t) r^2$ , and the volume linear depolarisation ratio,  $D(r, t)$ ).

170 The whole Alicenet data processing chain is developed for CHM15k systems since, as mentioned above, these were the ones  
171 firstly implemented in the network. It includes pre-processing procedures (cloud screening, denoising, overlap correction;  
172 Sect. 3.1), the absolute calibration (to determine  $C_L$  and, in turn,  $\beta_{\text{att}}$ ; Sect. 3.2), the quantitative retrieval of aerosol optical ( $\beta_p$   
173 and  $\alpha_p$ ) and physical (surface area,  $S_p$ , volume,  $V_p$ , and mass concentration,  $M_p$ ) properties (Sect. 3.3), and the automatic  
174 identification of main aerosol layers (continuous and mixed, CAL and MAL, and elevated, EALs, aerosol layers; Sect. 3.4).  
175 A similar full inversion chain is under development for CL61 systems, for which data processing is currently limited to the  
176 cloud screening and denoising, the absolute calibration (to monitor the stability of the instrument calibrated by the  
177 manufacturer), and the identification of aerosol layers (Fig. 2). Exploiting the CL61 depolarisation measurements (e.g.,  
178 Tesche et al., 2009), for these systems, the aerosol type dominating within each detected layer is also estimated (see Sect.  
179 3.4). For clarity, in Fig. 2 different colours are used to indicate Alicenet inputs, inversion steps, and outputs valid for  
180 CHM15k only (light green), for CL61 only (cyan), or for both (dark green).

181





182

183 **Figure 2:** Scheme of the Alicenet processing chain of the raw (L0) data and relevant output data products (L1-L3). The different colours in  
 184 the processing box are used to indicate inversion steps valid for CHM15k (light green), CL61 (cyan), or both (green) system types. This  
 185 same colour code is used for relevant output data products, which are further coloured from light to dark orange indicating processing  
 186 level, from the more basic (L1) quantities (altitude dependent Range-Corrected Signal, RCS, and depolarisation, D), through the attenuated  
 187 backscatter  $\beta_{att}$  (L2) to the optical and physical aerosol properties and aerosol layering (L2 & L3), see text for further details.

188

189 The Alicenet processing chain is completely automatic and centralised at CNR-ISAC. This setup allows the continuous  
 190 monitoring of the aerosol distribution across Italy, with L1 and/or L2 information accessible in near-real time through a  
 191 dedicated website (<https://www.alice-net.eu/>, last access: 7 March 2024). Some selected examples of this monitoring  
 192 capability are provided in Sect. 4. The more advanced, homogeneous and quantitative retrieval of aerosol properties and  
 193 layering across the network (L3 products) is conversely performed in post-processing and is not yet provided through the  
 194 Alicenet webpage.

### 195 3.1 Pre-processing

196 The first pre-processing steps are aimed at a) avoiding cloud/precipitation contamination in aerosol retrievals, and b)  
 197 tackling the signal noise (Sec. 3.1.1). Then the data need to be corrected for overlap artefacts (Sec. 3.1.2) before proceeding



198 with the determination of the instrument-specific calibration coefficient (Sec. 3.2). The way these preliminary steps are  
199 performed within Alicenet is described hereafter.

### 200 **3.1.1 Cloud-screening and denoising**

201 At the ALC laser wavelengths (near infrared), the reflectivity and optical thickness of clouds produce complete extinction of  
202 the laser beam above the cloud base. Only in case of thin clouds is the laser beam partially transmitted above the cloud base,  
203 but the return signal has a too low SNR to be employed for aerosol retrievals. The cloud-screening applied to the Alicenet  
204 data exploits the Cloud Base Height (CBH) identified by the ALC firmware (e.g., for CHM15k refer to  
205 <https://www.lufft.com/>, last access: 7 March 2024). In Alicenet, all data above an altitude of CBH - 500 m are filtered out,  
206 thus avoiding both the presence of cloud droplets and possible virga effects frequently observed below the cloud base. This  
207 also limits the impact of some variability in the CBH identification depending on the instrument type and firmware version.  
208 A temporal cloud-filter is also further applied, this removing profiles collected 15 min before-to-15 min after the firmware  
209 cloud detection. Some examples of the cloud screening applied to Alicenet ALC signals are reported in the Supplement  
210 (Sect. S1).

211 After the cloud-screening (if needed), the profiles are downscaled and denoised to improve accuracy of the aerosol retrievals.  
212 Indeed, as mentioned above, the ALC signal is generally collected with high temporal and vertical resolution and is affected  
213 by a decrease of the SNR along the profile. The denoising is performed by computing signal mean and standard deviation  
214 over specific time and range windows, and filtering those data where the SNR (defined as the ratio between the mean and the  
215 standard deviation) is below a given threshold. A minimum SNR of 20% is generally set for aerosol retrievals within  
216 Alicenet, while the resolution of the downscaled data is modulated depending on the time scales of the processes to be  
217 investigated. It may range from 1 min for the investigation of boundary layer dynamics (as done for the identification of the  
218 mixed aerosol layer) up to 30 min or 3 hours for the identification of aerosol loaded/free regions in the upper troposphere (as  
219 done for the identification of elevated aerosol layers or within the absolute calibration procedure, respectively).

### 220 **3.1.2 Overlap correction**

221 For CHM15K systems, an overlap correction of the signal in the near range (0-1000 m a.g.l.) is required. This is particularly  
222 important when ALC data are used for surface AQ applications, and especially in those conditions in which particulate  
223 matter is confined in the lowermost atmospheric levels. An instrument-dependent, time-invariant overlap function  
224 accounting for the signal loss is generally provided by the manufacturer ( $Ovl_{man}(r)$ ). However, it has been demonstrated  
225 (Hervo et al., 2016) that changes in the instrument sensitivity rather require the use of a temperature-varying overlap  
226 function. Within Alicenet, the derivation of such an overlap function is based on the procedure developed by Hervo et al.  
227 (2016) to which the reader is referred to for full details. This procedure firstly selects time windows in which it can be  
228 reasonably assumed to have an homogeneous aerosol layer down to the surface. Then, for those selected time windows, the



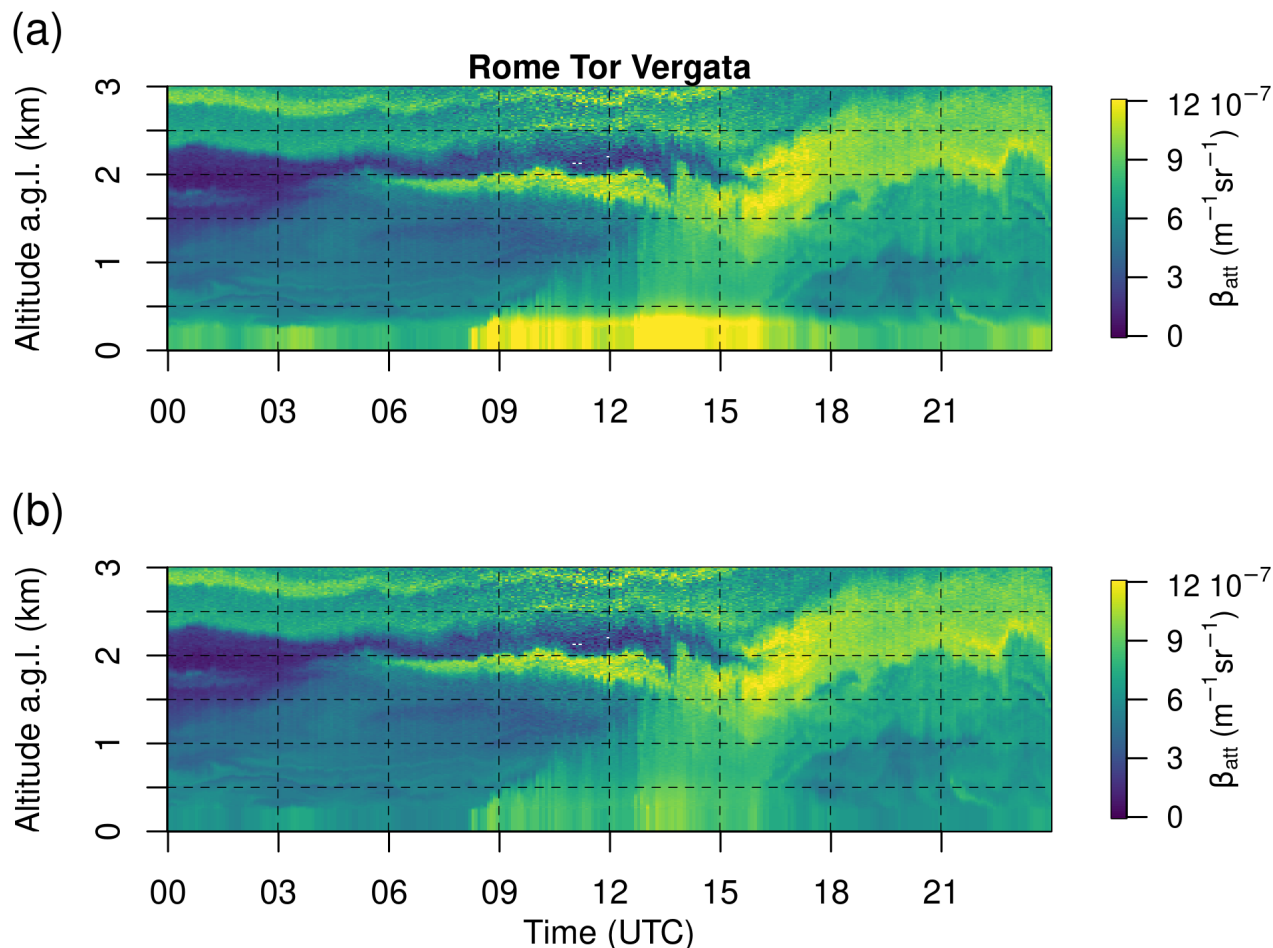
229 homogeneity of the ALC signal is forced down to the ground so to derive the overlap correction factor ( $f_c(r)$ ) to be applied to  
230 the manufacturer overlap function. As found by Hervo et al. (2016),  $f_c(r)$  is actually dependent on the system internal  
231 temperature. Therefore, to take this dependence into account, an ensemble of overlap correction factors is derived using a  
232 reasonably long dataset (generally spanning different months), and each  $f_c(r)$  is put in relation (linear fit) with the median  
233 internal temperature of the system ( $T_m$ ) within the corresponding time interval. The result is a range- and temperature-  
234 dependent ‘overlap model’  $Ovl(r,T)$ . Examples of such overlap models obtained for some Alicenet sites are given in the  
235 Supplement (Sect. S2).

236 Within Alicenet, some additional requirements and quality controls to the Hervo et al. (2016) procedure were introduced to  
237 derive a robust  $Ovl(r,T)$ :

- 238 a) since the assumption of aerosol homogeneity in the lowermost levels is rarely fulfilled at some stations, additional  
239 quality controls were introduced on the ensemble of  $f_c(r)$  in order to reject those likely derived in inhomogeneous  
240 conditions and thus leading to unrealistic overlap corrections (details are provided in the Supplement, Sect. S2);
- 241 b) the instrument-dependent overlap models are derived considering at least a 1-year datasets to reach a statistically  
242 significant ensemble of overlap functions spanning a representative range of temperature;
- 243 c) the overlap correction is only applied above 225 m a.g.l., to avoid altitude ranges where the partial overlap is still  
244 insufficient to derive quantitative information. Below this altitude, the profiles are extrapolated down to the ground  
245 either by linear fitting (applied for winter data, using the first four corrected ranges > 225 m) or assuming an  
246 homogeneous profile (applied for summer data).

247 As an example of the effects of overlap corrections, in Fig. 3 the 24h  $\beta_{att}$  profiles derived using (a) the overlap correction  
248 provided by the manufacturer and (b) the Alicenet overlap correction are shown (site: Rome-Tor Vergata, date: 12 August  
249 2019). This case was selected because of the high diurnal variation (15 K) of the system internal temperature. It is evident  
250 that the temperature-dependent overlap model is effective in correcting the false-gradient and the aerosol overestimation in  
251 the lowermost 500 m that the manufacturer function was not able to remove.

252



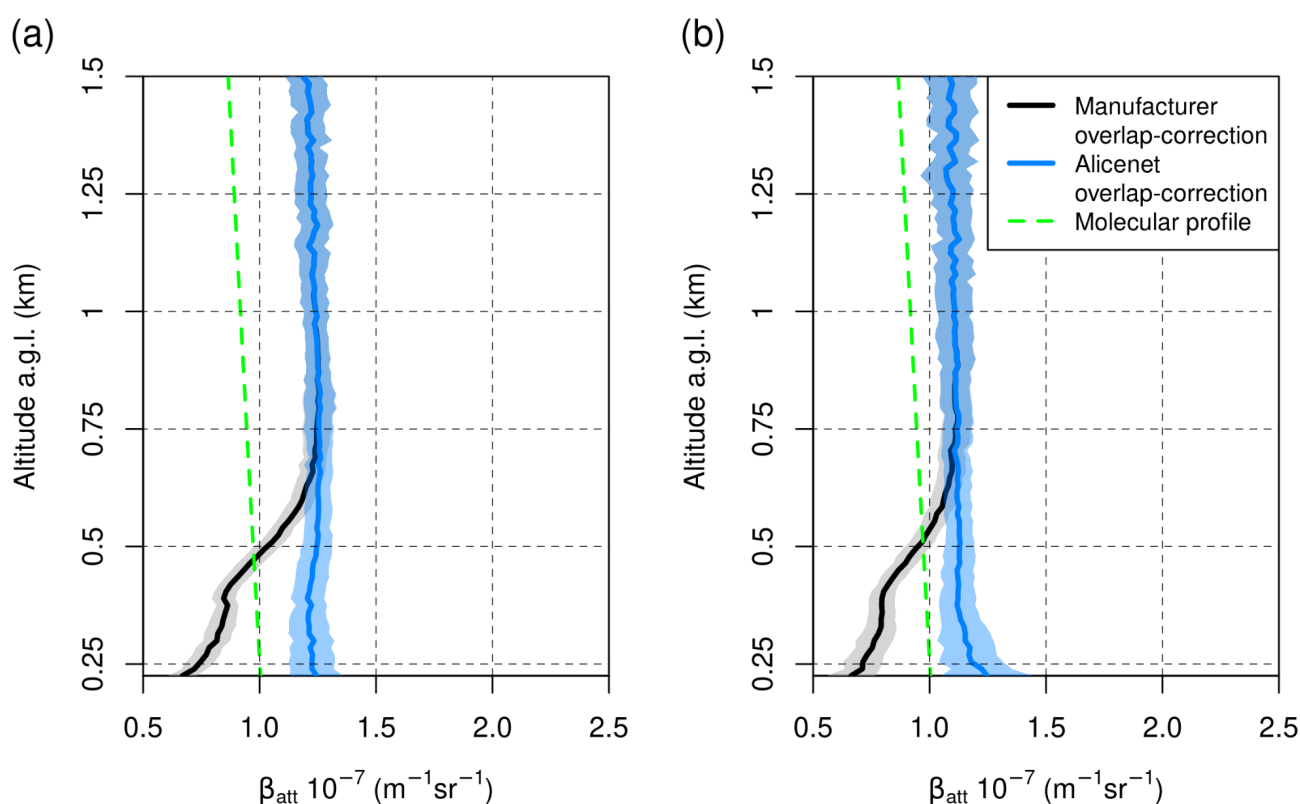
254 **Figure 3:** Overlap-corrected ALC profiles using: (a) the manufacturer overlap correction, and (b) the Alicenet overlap correction (data  
 255 referring to Alicenet Rome-Tor Vergata site on 12/08/2019).

256

257 A further effort to evaluate the ability of this procedure to provide a reliable overlap correction was conducted in the  
 258 mountain site of Aosta, exploiting the clean, nearly-molecular conditions often registered at this pre-alpine station. In fact,  
 259 due to its location, Aosta is frequently characterised by relatively low aerosol concentrations in the lowermost levels, these  
 260 conditions being mainly registered during Föhn events. This makes it possible to compare the overlap-corrected  $\beta_{att}$  profiles  
 261 with a theoretical molecular profile at very low altitudes. To perform this exercise, Föhn-related aerosol-free conditions of 3-  
 262 to-6 hours were identified by exploiting ancillary aerosol data (namely, surface PM10 concentrations measured by an OPC,  
 263 sun photometer-derived Aerosol Optical Depth, AOD) and meteorological parameters (wind, pressure, RH) from the AQMN  
 264 of ARPA Valle d'Aosta (Diémoz et al., 2021). For each of these selected cases, the mean  $\beta_{att}$  profiles retrieved using both the



265 manufacturer overlap correction and the Alicenet overlap correction were compared with a theoretical molecular profile.  
266 Figure 4 shows results for two cases (referring to 25 May 2021 and 6 October 2021) characterised by different values of the  
267 instrument internal temperature (308 K and 292 K, respectively) and low aerosol loads both at the surface ( $PM_{10} < 6$  and  $5$   
268  $\mu g m^{-3}$ , respectively) and along the column (AOD at 1200 nm  $< 0.04$  and  $0.03$ , respectively).  
269



271 **Figure 4:**  $\beta_{att}$  profiles derived using the manufacturer overlap correction (black line) and the Alicenet overlap correction (blue line) in two  
272 nearly-molecular conditions registered in Aosta on: (a) 25 May 2021 (5-8 UTC), and (b) 6 October 2021 (9-12 UTC). The shaded areas  
273 represent the  $\beta_{att}$  standard deviations within the selected time windows. The theoretical, molecules-only  $\beta_{att}$  profile is also reported (green  
274 line).  
275



276 Overall, the results show that the Alicenet overlap correction for the CHM15k in Aosta allows to reproduce the nearly-  
277 homogeneous, nearly-molecular  $\beta_{\text{att}}$  profiles expected in the lowermost levels ( $< 1500$  m), and to avoid unphysical values  
278 (lower than the molecular profile).

### 279 3.2 Absolute calibration

280 The absolute calibration (i.e., derivation of the calibration coefficient  $C_L$  in Eq. 1) is required to convert the pre-processed  
281 signal into quantitative aerosol information. For CHM15k systems, generally characterised by a SNR  $> 20\%$  up to 6-7 km,  
282 the absolute calibration procedure is performed by comparing the ALC signal with a theoretical molecular profile (Rayleigh  
283 calibration; Klett, 1985) in aerosol-free atmospheric regions (generally in the mid-upper troposphere). The theoretical  
284 molecular backscatter profile at the operating wavelength is derived based on temperature and pressure data (Bodhaine,  
285 1999). Within Alicenet we use site-dependent monthly averaged profiles of these variables, extracted from ERA5 reanalyses.

286 This calibration procedure, which is fully automatic, takes as input the pre-processed ALC signals and is made in two steps:  
287 a) search for the best-suitable molecular window, and b) computation of the calibration coefficient. The procedure builds on  
288 the E-PROFILE algorithm (<http://www.eumetnet.eu/activities/observations-programme/current-activities/e-profile/>, last  
289 access: 06-03-2024), although Alicenet introduced some specificities and quality controls in both steps as detailed below.

290 a) The selection of the molecular window is performed during nighttime (this avoiding sunlight noise) using vertical profiles  
291 collected over 3-6 hours (depending on cloudiness) at altitude ranges of 3-7 km altitude. Along this vertical range, an  
292 iterative procedure considers a fine grid of ‘potential’ molecular windows centred at different altitudes and with variable  
293 amplitudes (from 600 to 3000 m, at steps of 30 m). For each potential range-window (i.e. combination of central altitude and  
294 amplitude), the linear fit between the time-window-averaged signal and the theoretical molecular attenuated backscatter  
295 profile is performed. In order to reject the range-windows affected by aerosol layers, a test is performed to check for the  
296 presence of coherent structures therein. More specifically, the Breusch-Godfrey test (BG test; Breusch, 1978) is applied to  
297 calculate the autocorrelation in residuals, and the windows associated with high autocorrelation (i.e., p-value of the BG test  $>$   
298 0.05) are rejected. The molecular window selected from the ensemble of retained windows is the one maximising a specific  
299 metric which takes into account both the adjusted  $R^2$  and the intercept of the linear fit (details are reported in the Supplement,  
300 Sect. S3). The following two quality controls are then performed:

- 301 - The first quality control (QC1) assures that the linear fit slope is positive and the intercept nearly 0;
- 302 - There might be cases in which an undetected homogeneous aerosol layer within the range-window leads to a  
303 misleading robust linear regression with the molecular profile. A second quality control (QC2) is thus applied to  
304 filter range windows indicating the presence of an aerosol layer within their boundaries (details are reported in the  
305 Supplement, Sect. S3).

306 If these are not met, the night is rejected for calibration purposes, and the process continues using data from the following  
307 day.





308 b) Once the quality controlled molecular window is selected from the procedure above, the backward Klett inversion is used  
309 for the inversion of the time-averaged ALC signal to obtain the  $\beta_{\text{att}}$  profiles following Wiegner and Geiß (2012; 2014). Note  
310 that the sign correction in the Klett algorithm reported by Speidel and Vogelmann (2023) was already introduced in the  
311 Alicenet procedure. The  $C_L$  is then derived as:

$$312 \quad C_L = \frac{P(r) \frac{r^2}{Ovl}(r)}{\beta_{\text{att}}(r)} \quad (3)$$

313 Where the overbar denotes the median along the identified aerosol-free (molecular) range-window.

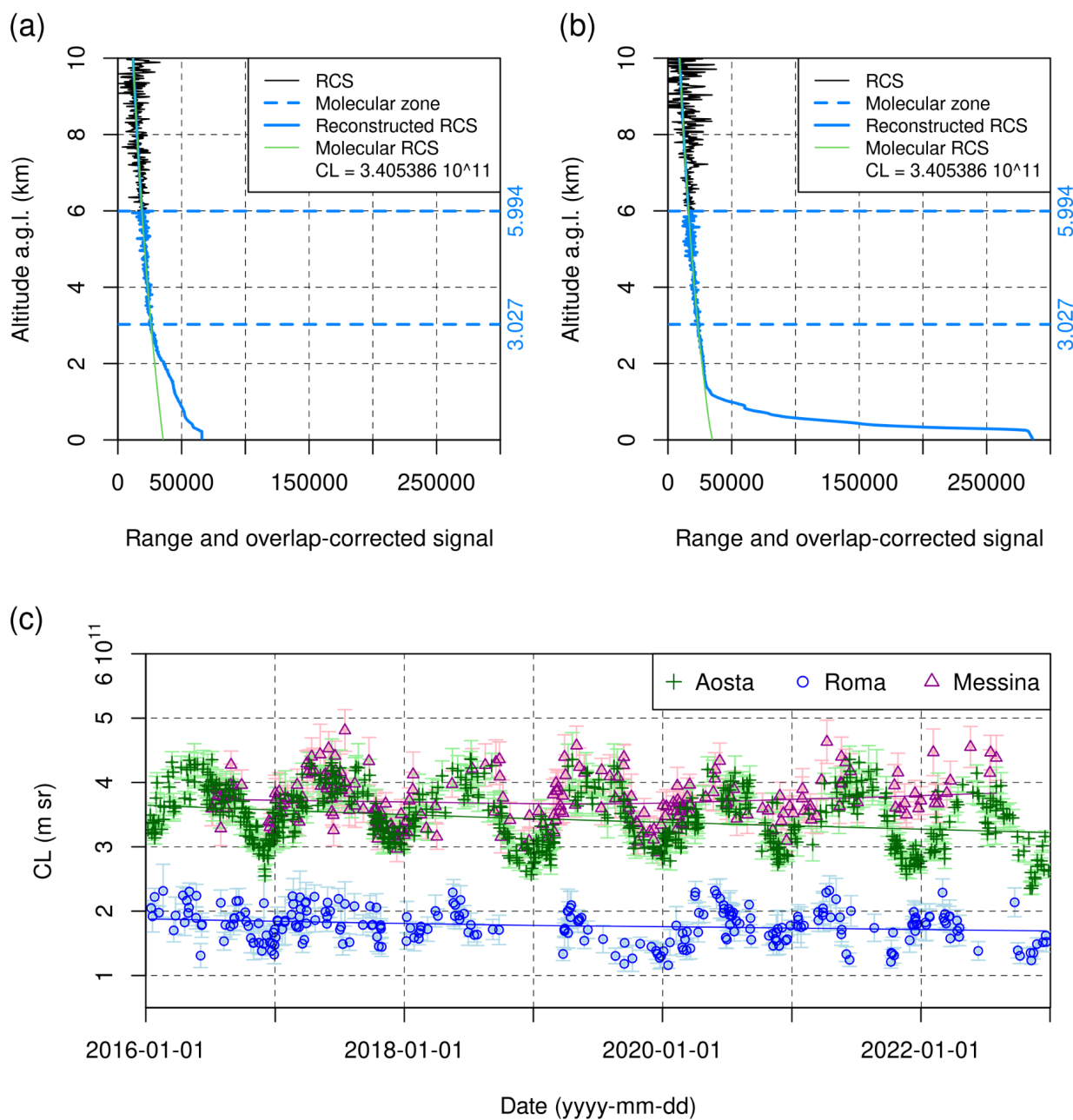
314 Two further quality controls are then performed at this stage:

- 315 - A third quality control (QC3) rejects the calibration coefficients for which the uncertainty exceeds a given threshold  
316 (see the definition of the  $C_L$  uncertainty and the threshold value in the Supplement (Sect. S3);
- 317 - Since the derived aerosol extinction coefficient can assume slightly negative values if the selected molecular  
318 window contains a non-negligible amount of aerosols, a last quality control (QC4) filters those calibrations  
319 associated with a negative sign of the AOD in the atmospheric layer 0-4 km resulting from the Klett inversion.

320 Figure 5 (top panels) shows two examples of successful calibrations, referring to the Alicenet ALC system operating in  
321 Aosta, during the nights of 21 May and 25 October 2017, respectively. The selected spring (autumn) nighttime calibrations  
322 correspond to a  $C_L$  close to the maximum (minimum) value of the year 2017. This can be verified in Fig 5c, showing the 7-  
323 year  $C_L$  time series (2016-2022) derived for the Alicenet CHM15k systems operating in Aosta, Rome and Messina (i.e.,  
324 Northern, Central and Southern Italy, respectively).

325 It is evident from Fig. 5c that the three series feature a similar seasonal cycle, as also observed in other European sites  
326 (<https://www.probe-cost.eu/resources/>, last access: 7 March 2024). The reason for such a cycle is not clear yet, and is  
327 currently under investigation. Main hypotheses are this cycle being related to instrumental issues (e.g. temperature-related)  
328 and/or to atmosphere-related phenomena. Different initiatives within the EC Cost Action PROBE, in which Alicenet is also  
329 involved, are currently ongoing to shed light on this seasonality. As reported by PROBE released documents, an undetected  
330 500nm-AOD of 0.02 within the calibration window would be sufficient to perturb the calibration coefficient up to 30%, i.e.,  
331 the maximum amplitude of the seasonal cycle observed in Aosta and Messina. Such an increase of the AOD within the  
332 calibration window is indeed plausible in spring and summer due to convection, large scale transport processes, and  
333 photochemical reactions.

334



336 **Figure 5:** (a, b) Examples of output of the Alicenet calibration procedure (nighttime signals of the Aosta CHM15k on 21 May and 921  
 337 October 2017, respectively) with indication of the molecular zones selected, and derived CL values. (c) Long-term (2016-2022) time series



338 of the calibration coefficients ( $C_L$ ) derived for the CHM15k systems operating in Aosta, Rome, and Messina, and associated Loess fits  
339 (lines) used to derive the actual CL values used in the operational, all-year-round data-inversions.

340

341 Due to the unclear reason for the variability of the calibration coefficients, at present the  $C_L$  values operationally used within  
342 Alicenet for the site-and day-specific aerosol retrievals are derived through a locally weighted smoothing (Loess) fit with a  
343 time span  $> 1$  year, thus flattening the seasonal variability but following long term trends related to instrument ageing (Fig.  
344 5c). It is important to underline that a different treatment of this variability could be necessary once the main driver of the  $C_L$   
345 seasonality is better identified. The uncertainty in the aerosol retrievals resulting from the  $C_L$  variability is discussed in Sect.  
346 3.3.3.

### 347 3.3 Retrieval of aerosol properties

348 This section describes the Alicenet inversion of the aerosol optical (Sect. 3.3.1) and physical (Sect. 3.3.2) properties.  
349 Specific examples of retrievals at the different Alicenet sites are also given and compared to a series of independent datasets  
350 in order to evaluate the relevant retrieval procedure performances.

#### 351 3.3.1 Aerosol optical properties

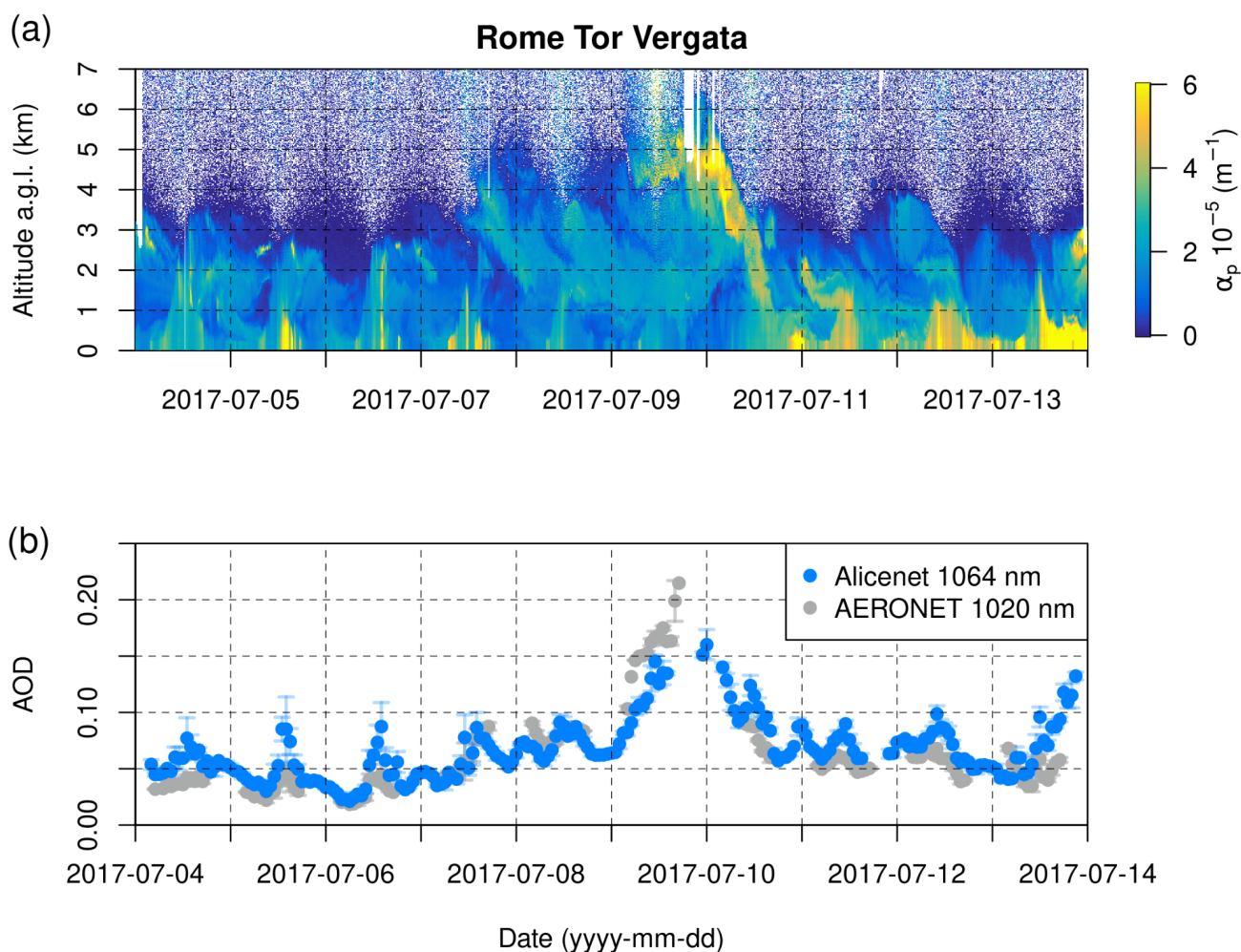
352 The aerosol backscatter ( $\beta_p$ ) profile is calculated from the total attenuated backscatter ( $\beta_{att}$ ) profile based on the forward Klett  
353 inversion (Wiegner and Geiß, 2012; 2014) of Eq. 1. Since both aerosol extinction and backscatter are unknown in Eq. 1, an  
354 assumption on the relationship linking the two variables is necessary to solve the Klett inversion. Within Alicenet, we do not  
355 fix an a priori, vertically-constant extinction-to-backscatter ratio (also referred to as lidar ratio, LR), as often done in elastic  
356 lidar retrievals. Instead, the aerosol extinction is assumed to be linked to backscatter through a specific functional  
357 relationship ( $\alpha_p = \alpha_p(\beta_p)$ ). This was obtained at the CHM15K operating wavelength (1064 nm) using a continental-type aerosol  
358 model as described in Dionisi et al. (2018). More specifically, an iterative procedure is used to derive  $\beta_p(r)$  and  $\alpha_p(r)$  vertical  
359 profiles. A first-guess uniform LR profile of 38 sr (similar to the value used in the NASA-CALIPSO inversion at 1064 nm  
360 for clean/polluted continental aerosol; Omar et al., 2009) is used in the first iteration step, and this first guess is then updated  
361 at each iteration using the  $\beta_p$  and  $\alpha_p = \alpha_p(\beta_p)$  profiles (i.e., the modelled functional relationship) until the  $\beta_p$  profile stabilises  
362 (i.e., the difference of the vertically integrated aerosol backscatter, IAB, in two successive iterations is  $< 0.0025 \text{ m}^{-1} \text{ sr}^{-1}$ ).

363 A way to check the performance of the ALC-based optical properties retrievals is to compare the relevant tropospheric  
364 integral of the aerosol extinction to the columnar AOD measured by an independent, co-located photometer. Within  
365 Alicenet, these comparisons were performed over both short- and long- term datasets thanks to some co-located AERONET  
366 (<https://aeronet.gsfc.nasa.gov/>, last access: 7 March 2024) or SKYNET (<https://www.skynet-isdc.org/>, last access: 7 March  
367 2024) sun-photometers within the network. Specific examples are shown in Figs. 6 and 7, respectively.



368 Figure 6a shows the aerosol extinction profiles derived from the Rome-Tor Vergata ALC during the EMERGE-EU field  
 369 campaign in July 2017 (Andrés Hernandez et al., 2022), while in Fig. 6b the corresponding ALC-derived AOD is compared  
 370 to the same quantity from a co-located AERONET sun photometer in Rome-Tor Vergata.

371



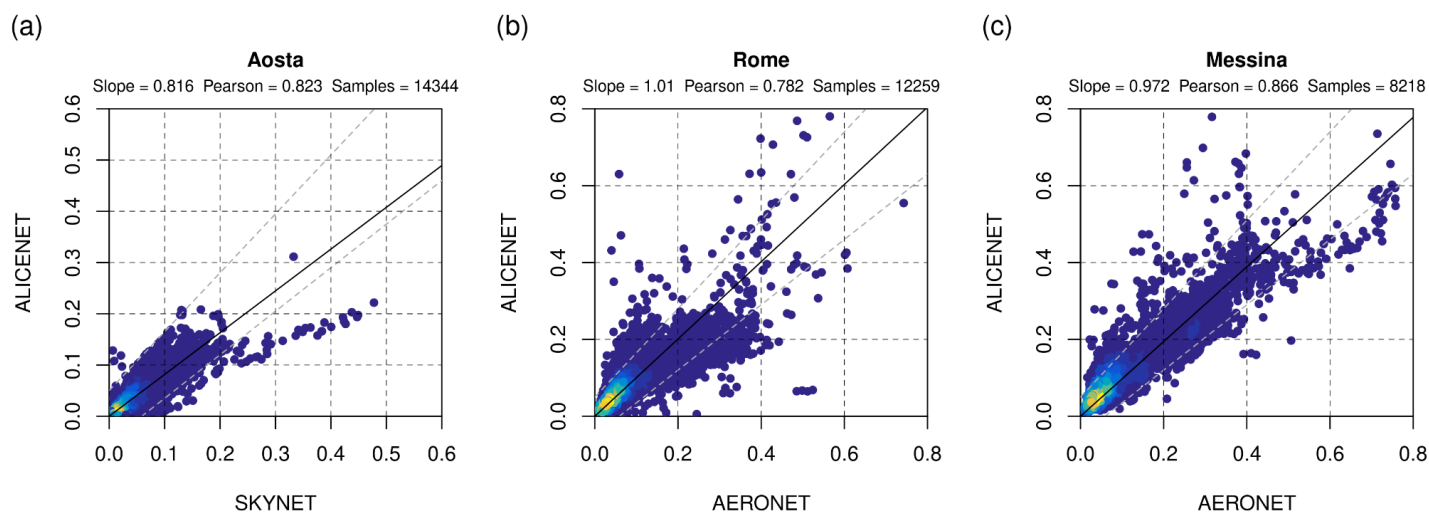
373 **Figure 6:** (a) Aerosol extinction profiles in Rome-Tor Vergata retrieved by the ALC Alicenet inversion during the EMERGE campaign in  
 374 July 2017, and (b) comparison between the relevant Alicenet- AOD and the co-located AERONET one (L2 data). Both Alicenet and  
 375 AERONET AODs are hourly averaged (error bars are the AOD standard deviations within this averaging interval).

376

377 The time series of the two independent datasets (both averaged at an hour resolution) agree within the expected uncertainties  
 378 (for AERONET, refer to Giles et al., 2019; for Alicenet, see Sect. 3.3.3). Some underestimation of the Alicenet retrieval is



379 found during the dates affected by transport of Saharan dust (e.g., 9 July 2017). This is expected because, as mentioned, the  
 380 functional relationship employed in the inversion was optimised for a continental-type aerosol and does not properly  
 381 describe the aerosol-to-extinction relation in desert-dust conditions (e.g., Barnaba and Gobbi, 2001). The extension of the  
 382 Alicenet retrieval approach to other aerosol types and relevant testing is planned for the future, also taking advantage of the  
 383 depolarisation measurements capabilities of the Vaisala CL61 operational within the network.  
 384 A more extended AOD comparison is shown in Figure 7, this exploiting a 7-year long (2016-2022) and multi-site (Aosta,  
 385 Roma, Messina) ALC and sun-photometers co-located dataset. In particular, AOD data were averaged at 15-min resolution  
 386 and matched in time (i.e., time differences < 5 min). In Aosta, the SKYNET AOD was derived taking into account the  
 387 temperature correction of the POM-02 photometer as described in Uchiyama et al. (2018). Figure 7 shows that the Alicenet  
 388 retrieval is able to quantify the actual aerosol load in a variety of conditions. Some ALC overestimations are mainly due to  
 389 instrumental noise in the upper troposphere, while underestimations are mainly related to the presence of non continental  
 390 aerosol types. This is better illustrated in the Supplement S3 (Fig. S3), where the same results are shown highlighting data  
 391 associated with Angstrom Exponents < 0.5 (as derived from the co-located photometers), associated to coarse-mode  
 392 dominated aerosol types, as desert dust or sea-salt particles.  
 393



395 **Figure 7:** Comparison between the AOD derived by Alicenet (at 1064 nm) and AERONET/SKYNET sun photometers (at 1020 nm) in (a)  
 396 Aosta, (b) Rome Tor Vergata, and (c) Messina over the 2016-2022 dataset. Colours refer to the data density. Black line is the linear fit. Fit  
 397 slope and Pearson’s correlation coefficients are reported in each panel together with the total number of data pairs (samples). Gray dashed  
 398 lines indicate a AOD-Alicenet deviation to the 1:1 line of  $\pm 0.01 \pm 0.15 \times \text{AOD}_{\text{sunphotometer}}$ .



399

### 400 3.3.2 Aerosol physical properties

401 An approach similar to the one used in the retrieval of the optical properties (Sec 3.3.1) is also used to derive aerosol  
402 physical properties. In fact, in the previous work by Dionisi et al. (2018) functional relationships linking the aerosol  
403 backscatter to the particle surface area and volume ( $S_p = S_p(\beta_p)$ ,  $V_p = V_p(\beta_p)$ ) for a continental-type aerosol are also provided.  
404 Aerosol mass concentrations ( $M_p$ ) can then be derived from the estimated aerosol volume as  $M_p = \rho_p V_p$ , using an a-priori  
405 aerosol density  $\rho_p$  value. To evaluate the performances of the aerosol physical properties retrievals, the Alicenet estimates of  
406 aerosol mass have been compared to in situ data. It is worth highlighting that remote sensing aerosol retrievals provide  
407 aerosol properties in ‘unperturbed’ atmospheric conditions, i.e., including hygroscopic effects. Conversely, most in-situ  
408 instrumentation (as those operating in AQMN in compliance to the EU AQ Directive) generally operates after drying the  
409 aerosol samples. Therefore a RH ‘adjustment’ of the ALC-based aerosol properties is necessary when the two are to be  
410 compared (e.g. Barnaba et al., 2010). For PM estimates, taking the in-situ (dry) measurement as reference, the ALC-derived  
411 ‘wet’ mass ( $M_p$ ) can be corrected to ‘dry’ aerosol mass ( $M_p^{dry}$ ) taking aerosol hygroscopicity into account.  
412 In Alicenet, the dry aerosol mass is estimated following Adam et al. (2012):

$$413 M_p^{dry} = \frac{M_p^{wet}}{1 + 1/\rho_d (GF^3 - 1)} \quad (4)$$

414 where

$$415 GF = \left(1 - \frac{RH}{100}\right)^{-\gamma} \quad (5)$$

416 is the hygroscopic growth factor. The dry aerosol density  $\rho_d$  and the  $\gamma$  exponent depend on the aerosol particles under  
417 investigation.

418 Here, both a short- (Fig. 8) and long- (Fig. 9) term comparison of the  $M_p$  retrieved by Alicenet with reference measurements  
419 are reported. The ALC datasets are from Aosta, which is one of the most tricky environments within Alicenet to deal with  
420 aerosol hygroscopic effects.

421 In the first case,  $M_p$  values at 3500 m a.s.l. (i.e., well above the region of incomplete ALC overlap) extracted from the ALC  
422 aerosol profiles are compared with in-situ aerosol concentrations measured by OPC at the same altitude (‘Testa Grigia’  
423 observatory, Plateau Rosa, 35 km-East of Aosta, see Supplement 4, Fig. S4) in June 2022. This period was selected because  
424 during summer aerosols (mostly secondary hygroscopic particles) from the Po Basin are regularly transported to the western  
425 Alps in thick layers, reaching altitudes  $> 4$  km a.g.l. (Diémoz et al., 2019 a,b) thus likely impacting the two sites in a similar  
426 way. In fact, June 2022 registered both long-range transport of desert dust and medium-range transport of Po Valley  
427 pollution to Plateau Rosa. For the comparison, the ALC-based mean aerosol volume in the vertical range  $3500 \pm 200$  m was

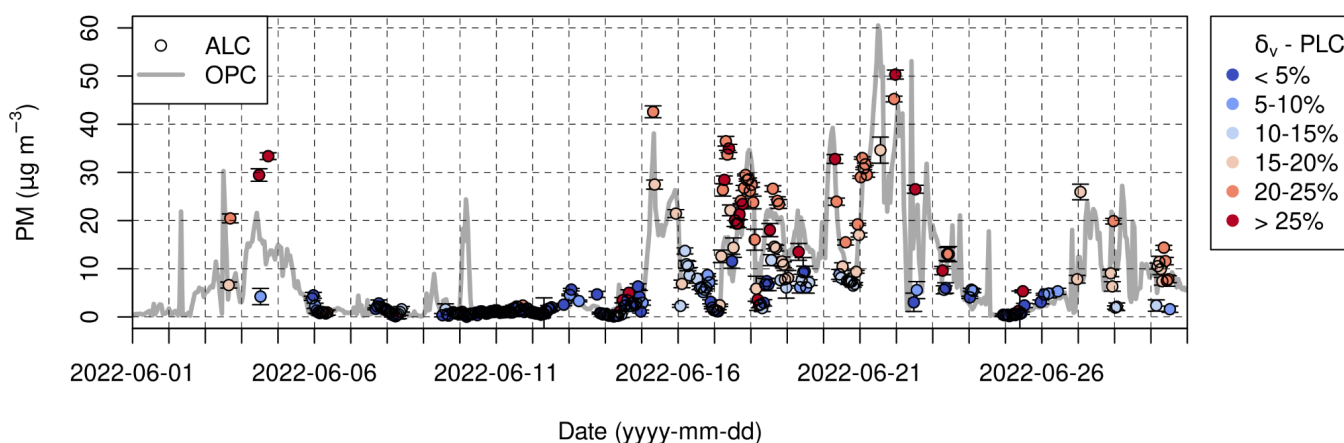




428 considered. A constant aerosol density of  $1.5 \text{ g cm}^{-3}$  was used to derive  $M_p$  values from both OPC- and ALC-based volume  
 429 concentrations. The ALC hygroscopic correction was only applied when the co-located PLC registered a linear volume  
 430 depolarisation ratio  $\delta_v < 15\%$  within this altitude range, thus avoiding the irregular and poorly hygroscopic dust particles. For  
 431 these particles, the  $\gamma$  exponent in Eq. 5 was setted to 0.2, as derived by D'Angelo et al. (2016). The modelled RH profiles  
 432 from MERIDA (Bonanno et al., 2019) were used in Eq 4.

433 Figure 8 shows the two mass estimates to exhibit a similar time evolution, with good agreement both in low aerosol  
 434 conditions (e.g. 6-15 June 2022), and during transport events increasing the local aerosol load, such as desert-dust intrusions  
 435 (e.g., 3-5, 18-22, and 27-28 June 2022) or Po Valley pollution advections (e.g., 13-14, and 25-26 June 2022). This result is  
 436 very promising, considering the horizontal distance between the ALC-probed column and the Plateau Rosa station ( $> 30 \text{ km}$ ,  
 437 Figure S4.2), and that the in-situ OPC measurements may also be influenced by local surface dynamics and emissions.

438



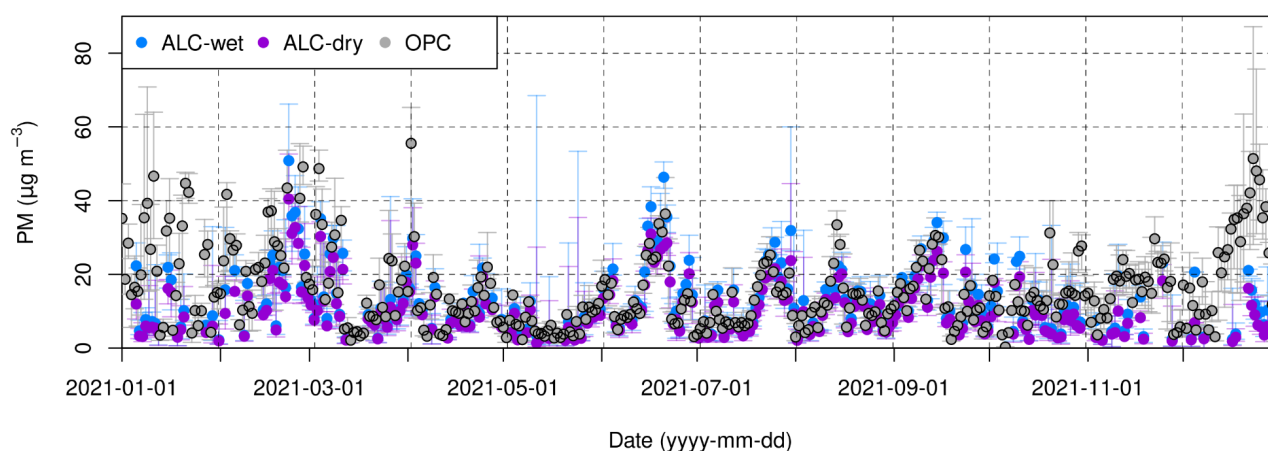
439 **Figure 8:** Aerosol mass concentrations derived from the Aosta ALC signals in the vertical layer  $3500 \pm 200 \text{ m a.s.l.}$  (bullets, colour code  
 440 relates to depolarisation values from the co-located PLC), compared with the in-situ  $\text{PM}_{10}$  concentrations derived from OPC  
 441 measurements (grey line) at the mountain observatory ‘Testa Grigia’ ( Plateau Rosa,  $3500 \text{ m a.s.l.}$ ) in June 2022 (OPC data courtesy of  
 442 Stefania Gilardoni, CNR-ISP, see also Figure S4 in the Supplement for details on site locations).

443

444 In Fig. 9, a 1-year (2021) comparison was performed using the Alicenet aerosol mass product  $M_p$  and the in situ, surface  
 445  $\text{PM}_{10}$  concentrations derived by OPC measurements in Aosta downtown (4 km from the Aosta-Saint Christophe ALC;  
 446 Diémoz et al., 2021). The aerosol density was set to  $1.5 \text{ g cm}^{-3}$ , and the ALC hygroscopic correction was applied using  
 447 surface-level RH measurements. Figure 9 shows the daily median values, and corresponding 25-75 percentiles, retrieved  
 448 from both datasets. As can be observed, the Alicenet retrieved  $M_p$  is able to reproduce the variability of the in-situ measured



449  $PM_{10}$ , with some underestimations in the winter months. These underestimations are mainly attributable to i) the shallow  
 450 (i.e., few tens of metres), frequent temperature inversions occurring during winter in the Alpine valleys and capping aerosols  
 451 in the lowermost levels (Giovannini et al., 2020), and ii) the higher wintertime local emissions in the urban site of Aosta  
 452 downtown with respect to the semi-rural site where the ALC is operating (Diémoz et al., 2019b).  
 453



455 **Figure 9:** Daily median values (and relevant 25-75 percentiles, vertical bars) of a one-year (2021) dataset of aerosol mass concentrations  
 456 as derived by the Alicenet ALC inversion (first vertical level of the ALC signal) and by in situ OPC measurements in Aosta.  
 457

### 458 3.3.3 Uncertainty of retrievals

459 Despite the efforts described above to exploit the great potential of ALC to retrieve quantitative data for a series of aerosol-  
 460 related geophysical parameters, and the good performances of the retrievals shown above, due to several factors, associated  
 461 uncertainties to the Alicenet-derived parameters keeps of the order of 30-40%. In fact, the main sources of uncertainty of the  
 462 retrieved aerosol properties are associated with: 1) the instrumental noise of the signal, 2) the overlap correction applied to  
 463 the signal, 3) the variability of the instrument calibration coefficient, and 4) the accuracy of the functional relationships in  
 464 terms of both internal uncertainty and their representativeness of the actual aerosol type sounded. The first factor depends on  
 465 the instrument status and impacts the retrieval mainly in the middle-upper troposphere. The second factor, impacting in  
 466 particular the lowermost levels, depends on the accuracy of the overlap correction, i.e., on the statistical and physical  
 467 representativeness of the ensemble of overlap functions from which the overlap model is derived (Sect. 3.1.2). The third  
 468 factor, derived as outlined in Sect. 3.2, directly impacts the accuracy of  $\beta_{att}$ . For example, it is found by propagation that



469 changes of 30% in the instrument calibration coefficient (which are quite usual in some Alicenet and E-PROFILE stations)  
470 may result in errors in  $\beta_{\text{att}}$  up to 20%. The fourth factor, impacting the accuracy of  $\alpha_p$ ,  $V_p$ , and, to a lesser extent,  $\beta_p$ , strongly  
471 depends on the actual aerosol conditions: the functional relationships used can give a good estimate of the aerosol properties  
472 in presence of continental aerosols, while in presence of non-continental particles they are less accurate (a relative error of  
473 30-40% was derived by Dionisi et al., 2018). As mentioned, extension of the Alicenet approach to include other aerosol  
474 types is foreseen for the next future, particularly exploiting the PLC depolarisation profiles for aerosol-typing, and thus  
475 driving selection of aerosol-type specific functional relationships (e.g. Gobbi et al., 2002).

476 Concerning the retrieval of aerosol mass concentrations, the assumed particle densities are a major source of uncertainty, and  
477 the accuracy of the retrieval depends on the possibility to better constrain the aerosol density profiles, e.g., through ancillary  
478 data, including depolarisation information.

479 Overall, the above factors result in time and range-dependent uncertainties of the ALC-based aerosol optical and physical  
480 properties. Their amplitude and vertical variability depend on the instrument characteristics (e.g., amplitude and shape of the  
481 signal noise), and on the actual aerosol composition and stratification. The expected uncertainty with an optimal SNR up to  
482 at least 7 km a.g.l., an overlap error < 10% in the lowermost levels, and in presence of continental aerosol types is of 30-40%  
483 for the AOD, reaching 50% for aerosol mass.

#### 484 **3.4 Automatic identification of aerosol layers**

485 In addition to the quantitative retrievals of specific aerosol properties, ALC measurements can also provide a simplified yet  
486 useful information on a key aspect of atmospheric studies, i.e., vertical stratifications, from the lowermost levels to the mid-  
487 upper troposphere, using aerosols as tracers.

488 Due to the influence of the Earth surface, in the lower troposphere the atmospheric stratification generally features a  
489 temperature inversion, capping locally emitted aerosols, trace gases and moisture. During daytime, the heating of the Earth  
490 surface triggers the development of turbulent fluxes, mixing the above quantities within the so-called Mixed Boundary Layer  
491 (MBL) and causing its growth by entrainment of upper air up to the capping inversion (Stull, 1988). In the mid-upper  
492 troposphere, atmospheric circulations drive large scale aerosol transport processes. The aerosol loaded air masses are  
493 generally advected above the MBL, but may descend and be entrained within it. It is worth mentioning that the aerosol  
494 stratification depends not only on local (mainly vertical) and synoptic (mainly horizontal) scale dynamics, but also on  
495 (horizontal and vertical) mesoscale circulations, in particular over complex terrain (Serafin et al., 2018; Collaud Coen et al.,  
496 2018). Moreover, stagnation, secondary aerosol formation, hygroscopic effects, and photochemical reactions can  
497 significantly modulate aerosol concentrations within specific atmospheric layers (Collaud Coen et al., 2011; Curci et al.,  
498 2015; Sandrini et al., 2015) making this scheme more complex to be interpreted. However, three main aerosol layer types  
499 can be generally identified:



- 500 a) a layer characterised by the continuous (in space and time) presence of aerosols (Continuous Aerosol Layer, CAL),  
501 as a results of a combination of factors, among which surface aerosol emissions, capping inversion effects,  
502 convection processes, secondary aerosol formation;
- 503 b) within the CAL, a layer where aerosols are mixed by surface-driven turbulent fluxes (Mixed Aerosol Layer, MAL),  
504 whose pronounced diurnal variability is mainly determined by local thermal forcings and, in certain sites, by  
505 mesoscale circulations transporting or removing particles in the lower troposphere;
- 506 c) aerosol layers detached from the surface (Elevated Aerosol Layers, EALs), above the MAL and either within or  
507 above the CAL, generally resulting from medium-to-long range advections, or from the development of the local  
508 residual layer during nighttime.

509 A novel, stand-alone procedure (ALADIN: Aerosol LAYer DetectIoN) was developed within Alicenet to extract and make  
510 this (CAL, MAL, and EAL) layering information usable within the network. This procedure is described hereafter, with  
511 examples of the products over the short and long term. It can be applied on both ALC and PLC.

512 A variety of methodologies have been developed to derive quantitative information on the aerosol layering from ALCs (e.g.,  
513 Haeffelin et al., 2012). These are based, for example, on the Continuous Wavelet Transform (CWT) analysis (Morille et al.,  
514 2009; Caicedo et al., 2020) or the detection of anomalies with respect to background aerosol conditions (Adam et al., 2020).  
515 Methods based on the variance and gradient analysis of ALC signals (e.g., Angelini et al., 2009; Poltera et al., 2017;  
516 Kotthaus et al., 2020) or image processing techniques (e.g., Vivone et al., 2021) have also been applied for the detection of  
517 the MBL height. It is worth mentioning that the MBL and MAL definitions should not be considered synonyms, since the  
518 first is based on thermodynamic quantities, while the second uses aerosols as tracers.

519 Within the Alicenet ALADIN procedure, the CAL height is derived from cloud-screened, denoised, and calibrated ALC  
520 profiles averaged at 30 min resolution. It is simply defined as the altitude of the layer in which  $\beta_{\text{att}} > \beta_{\text{mol}}$  for at least 98% of  
521 its extension.

522 The MAL is identified through a technique disentangling regions where aerosols are mixed by (vertical) turbulent fluxes  
523 from the ones where they are transported by (mainly horizontal) large-to-medium scale circulations. More specifically, the  
524 Dynamic Time Warping algorithm (DTW, Giorgino et al., 2009) is applied to a sequence of denoised  $\beta_{\text{att}}$  profiles at 1-min  
525 resolution. In brief, this algorithm computes the local stretch or compression to be applied to each profile in order to  
526 optimally map the preceding into the following. Its output field ( $w_{\text{DTW}}$ ) can be interpreted as the local vertical displacement  
527 of the aerosol-loaded air parcels, while the region near the surface where  $w_{\text{DTW}}$  rapidly changes in sign and magnitude as the  
528 region where the mixing is acting. In order to select this region, the standard deviation of  $w_{\text{DTW}}$  ( $w_{\text{SD}}$ ) is calculated over 30-  
529 min intervals (as generally done in Eddy-Covariance analysis; Aubinet et al., 1999) and the local minima along the  $w_{\text{SD}}$   
530 profiles are identified. The MAL height is then defined as the height of the first  $w_{\text{SD}}$  local minima verifying specific criteria  
531 (details are provided in the Supplement, Sect. S5). It is derived only when ALC profiles below 500 m a.g.l. are cloud-free.

532 The identification of the EALs is based on the CWT analysis followed by an iterative technique. More specifically, the  
533 identification of the layer ‘centre’ takes advantage of the CWT algorithm (MassSpecWavelet R package) developed by Du et



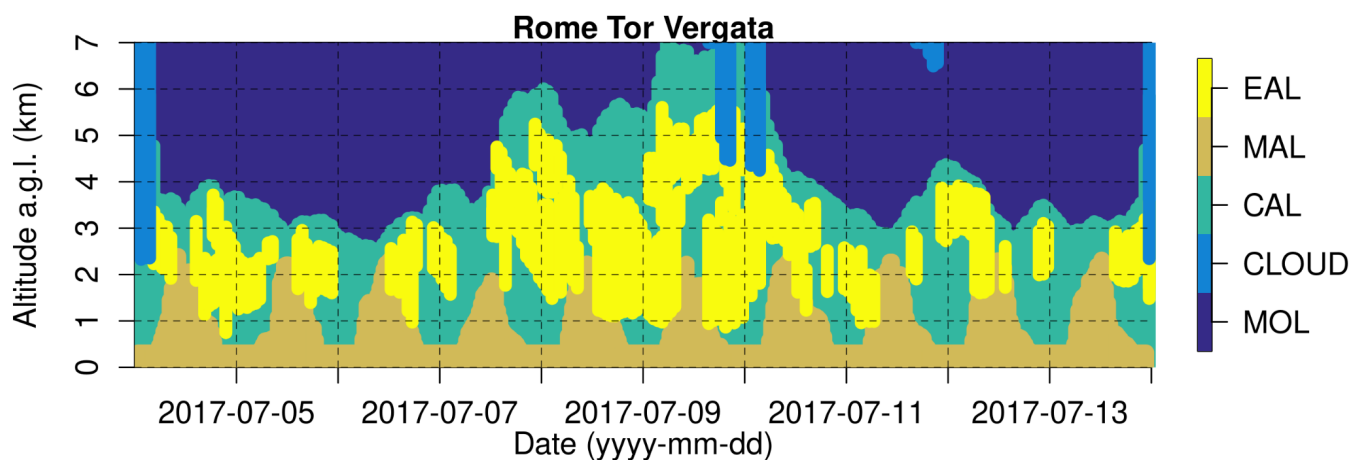
534 al. (2006), which is applied to cloud-screened and denoised  $\beta_{\text{att}}$  profiles at 30-min resolution. This algorithm exploits both the  
535 CWT and  $\beta_{\text{att}}$  coefficients to identify peaks attributable to aerosol layers and discriminates these from noise. Once an aerosol  
536 layer ‘centre’ is identified, its top and bottom boundaries are determined with an iterative procedure. More specifically, a  
537 grid of ‘potential’ bottom and top boundaries is constructed, and for each boundaries combination an ad hoc metric is  
538 calculated (it takes into account the deviation of the  $\beta_{\text{att}}$  profile with respect to a reference profile ( $\beta_r$ ), the integrated  $\beta_{\text{att}}$   
539 coefficients, and the CWT coefficients). The EAL is then identified as the window maximising this metric (details, including  
540 quality controls, are provided in the Supplement, Sect. S5). In this approach, the choice of the reference profile  $\beta_r$  to be used  
541 depends on the intended application: molecular attenuated backscatter profiles are used to detect aerosol layers with respect  
542 to a clean atmosphere, while ‘climatological’ profiles (e.g. site- and monthly-dependent median  $\beta_{\text{att}}$  profiles derived from  
543 Alicenet multi-annual datasets) are used to identify aerosol layers representing anomalies with respect to typical aerosol  
544 conditions. Mean properties of the EAL are also derived, and namely, the mean AOD, estimated using the aerosol extinction  
545 profiles from CHM15k systems, or the mean fraction of irregular (mainly dust) particles, estimated from the linear volume  
546 depolarisation ratio ( $\delta$ ) values of CL61 systems as follows (Tesche et al., 2009):

547 
$$F_d = \frac{\overline{(\delta - \delta_{nd})(1 + \delta_d)}}{\overline{(\delta_d - \delta_{nd})(1 + \delta)}} \quad (6)$$

548 where  $\delta_d$  and  $\delta_{nd}$  are the typical dust and non-dust volume depolarisation values (assumed as 0.25 and 0.05, respectively), and  
549 the overbar denotes the median within the bottom and top boundaries of the layer.

550 Figure 10 shows an example of the ‘layering mask’ derived from the overall ALADIN procedure, this referring to the same  
551 CHM15k data (Rome-Tor Vergata site) shown in Fig. 6. The mask discriminates between the vertical ranges characterised  
552 by the presence of aerosol layers (CAL, MAL, EALs), aerosol-free (i.e., molecular, MOL), and cloud-screened (CLOUD)  
553 regions. In this case, the EALs are identified using as reference profile ( $\beta_r$ ) the median summertime  $\beta_{\text{att}}$  profile derived from  
554 the multi-annual (2016-2022) dataset of the instrument. In the episode reported in Fig. 10, the elevated layers above 3 km  
555 a.g.l. are mostly due to Saharan dust advections, while the ones below 2-3 km a.g.l. to the development of the residual layer  
556 during the night (e.g., 5-6 July 2017), or the presence of fire plumes travelling in the lower troposphere (e.g., 11 July 2017).  
557 This further discrimination was made possible through the analysis of the depolarisation profiles of the prototype-CHM15k  
558 PLC in downtown Rome (not shown), and ancillary information (models, satellite). The inclusion of the CL61 depolarisation  
559 information directly within the layering procedure as outlined above represents a first step to automate the layer typing  
560 capacity within the network (e.g., Nicolae et al., 2018; Córdoba-Jabonero et al., 2018).

561



563 **Figure 10:** Atmospheric layering mask derived from the Alicenet ALADIN processing on the CHM15k operating in Rome - Tor Vergata  
 564 in the same period presented in Fig. 6. The mask discriminates the following layers: the continuous aerosol layer (CAL), the mixing  
 565 aerosol layer (MAL) and elevated aerosol layers (EALs), as well as aerosol-free, molecules-only regions (MOL) and clouds-affected  
 566 (CLOUD) vertical ranges.

567

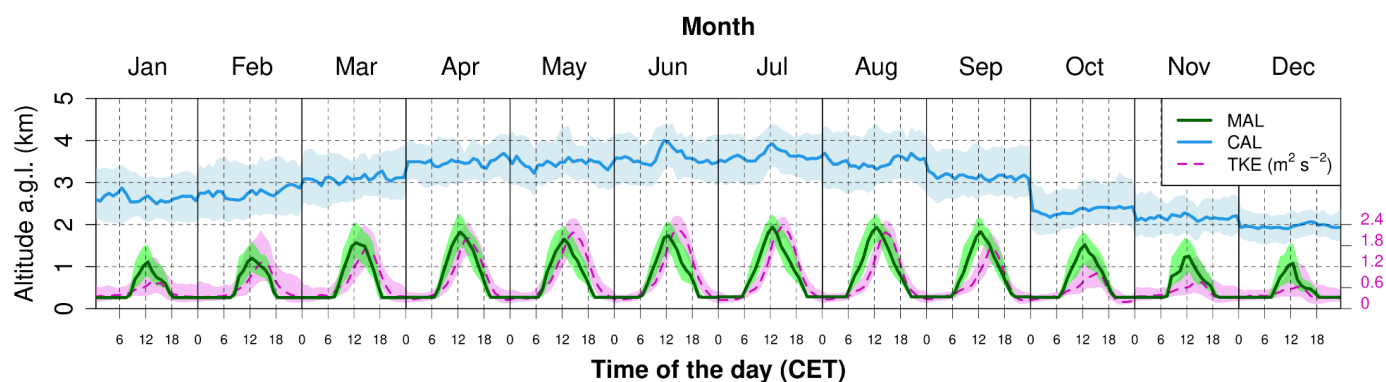
568 An example of the results derived from the application of the ALADIN procedure on a multiannual (2016-2022) ALC  
 569 dataset is given in Fig. 11. This shows the monthly-resolved statistics (median and 25-75 percentiles) of the CAL (cyan) and  
 570 MAL (green) daily cycles derived from the CHM15k dataset in Rome Tor-Vergata. The CAL parameter clearly shows an  
 571 yearly cycle (minimum in winter and maximum in summer) while its daily cycle is slightly different in winter (thicker  
 572 during the night, likely due to enhanced hygroscopic growth of particles) with respect to summer (thicker in the mid part of  
 573 the day, likely driven by enhanced convection). As expected, all over the year, the MAL shows a marked daily cycle, with  
 574 maximum heights in summer (about 2 km thick in July-August) doubling those in winter (about 1 km in December-January).  
 575 For direct comparison to the ALC-derived, aerosol-traced MAL, similar monthly- and daily- resolved statistics of turbulent  
 576 kinetic energy (TKE) data were also derived, using a co-located ultrasonic anemometer (magenta lines). Note that,  
 577 differently from the other Figures, in which time was always reported as UTC, in this case Central European Time (CET) is  
 578 used to better highlight the diurnal (a.m./p.m.) variability of the quantities addressed. As can be observed, the timing of the  
 579 moment the MAL starts increasing during the morning matches the TKE one, although the former grows faster, anticipating  
 580 its daily maximum with respect to the TKE one. This temporal shift is kept during the afternoon, especially in summer. This  
 581 is likely due to the fact that during the morning the ALC signal increases due to an increase of local aerosol emissions, and  
 582 not just due to turbulent energy-driven convection. In the opposite way, the typical land-sea breeze developing in Rome in





583 the early afternoon (Di Bernardino et al., 2022) acts in removing aerosol particles, thus leading to a decrease of the ALC-  
 584 based MAL estimation, while enhancing the mechanical component of the TKE, which in fact starts decreasing later in the  
 585 day.

586



588 **Figure 11:** Monthly and daily resolved statistics of the MAL and CAL heights (median, and 25-75 percentiles as dashed areas) derived  
 589 from the CHM15k in Rome Tor Vergata (2016-2022 dataset), with the relevant TKE statistics derived from a co-located ultrasonic  
 590 anemometer (violet line and dashed area).

591

592 A more detailed long-term and Alicenet multi-site analysis of aerosol properties and stratifications is in progress (Bellini et  
 593 al., 2024a).

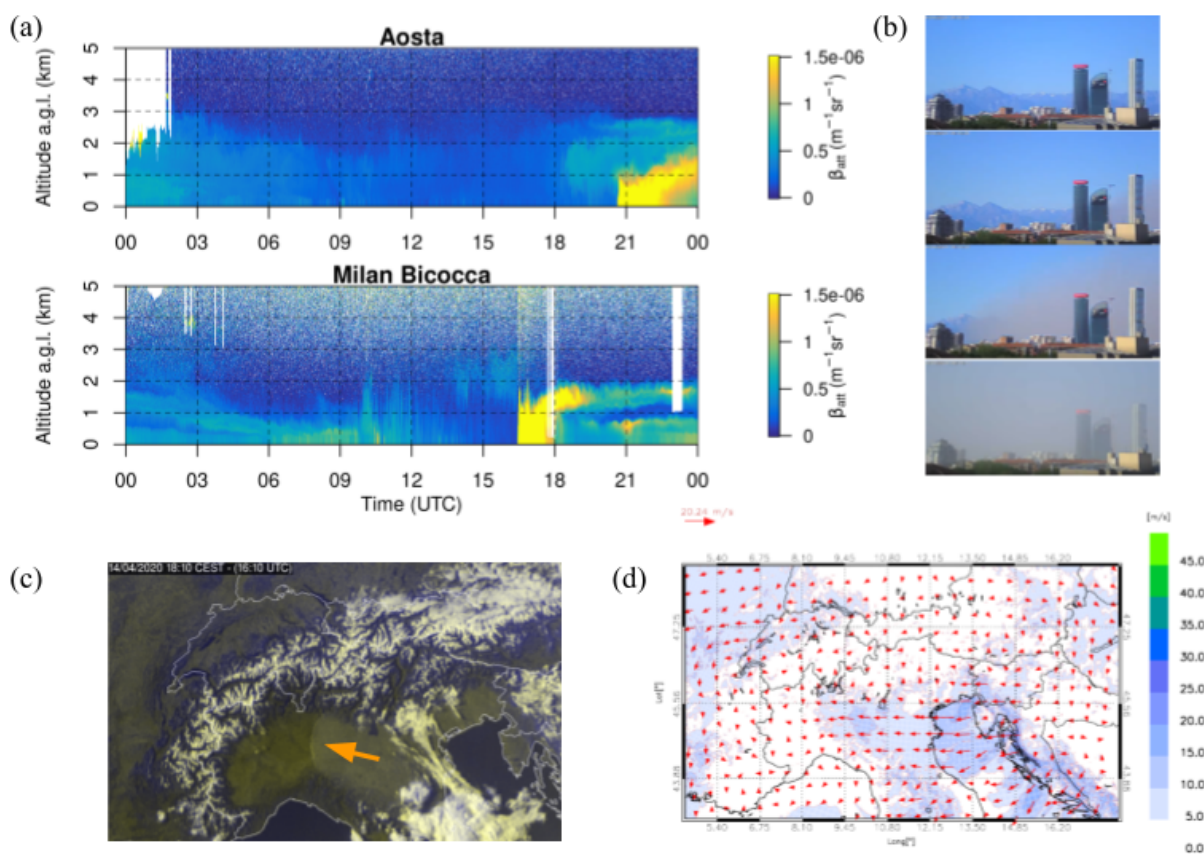
#### 594 4. Potential from 4D near-real time aerosol monitoring

595 The continuous monitoring capability of the Alicenet network has been already exploited in past events to characterise  
 596 specific aerosol transport features and/or to quantify the impact of aerosol dynamics on local aerosol concentrations, mostly  
 597 in synergy with other tools and measuring techniques as in-situ aerosol observations, ground-based passive remote sensors,  
 598 satellites or models (Gobbi et al., 2019; Diémoz et al., 2019a,b; Rizza et al., 2022; Tositti et al., 2022, Andres Hernandez et  
 599 al., 2022). This section describes, through some recently recorded showcases, the potential of the near real time Alicenet  
 600 monitoring at the national scale, that could also represent a useful tool for nowcasting/warnings/alerts in case of noteworthy  
 601 events.

#### 602 4.1 Po Valley local dust front (14 April 2020)



603 In a previous study (Diemoz et al., 2019a,b), the operational use of Alicenet provided observation-based evidence of the  
 604 export of pollutants from the Northern Italy Po Valley to surrounding areas. The phenomenon, previously observed by lidar  
 605 profiling performed at the EC-JRC in Ispra (about 60 km northwest of Milan, Barnaba et al., 2010), was further analysed  
 606 and quantified thanks to the Alicenet combination of sites (within and at the border of the Po Valley), demonstrating that  
 607 such advectations markedly affect PM-related AQ even in the ‘pristine’ mountain environments mainly transporting  
 608 hygroscopic particles of secondary origin. However, transport of particles of primary origin (particularly from soil-related  
 609 sources) across the Po Valley has been also observed, particularly during dry periods. Figure 12 shows an example of such  
 610 events (14 April 2020), largely impacting regional AQ and visibility.  
 611



613 **Figure 12:** (a) Total attenuated backscatter profiles at Aosta and Milan-.Bicocca sites on 14/04/2020; (b) central Milan webcam (Source:  
 614 Arzaga meteorological observatory, <https://www.osservatorioarzaga.it/>) showing the rapid decrease of visibility on 14/04/2020 (from top  
 615 to bottom: 16:08, 16:15, 16:20, 16:25 UTC), (c) Po Valley satellite true colour image (14/04/2020 18:10 UTC; Credits: EUMETSAT) with  
 616 indication of the regional dust front (orange arrow), and (d) 10 m wind speed and direction simulated by WRF over North Italy



617 (14/04/2020 17:00 UTC, data courtesy of Stefano Federico CNR-ISAC) illustrating the extension of the gust and wind fronts. The arrival  
618 of the dust front in Milan at 16:20 UTC and in Aosta at 20:40 UTC is clearly visible from ALC profiles.

619

620 In fact, anomalous dry conditions affected Europe in April 2020. ALC profiles in Aosta and Milan-Bicocca (Fig. 12a) clearly  
621 capture the timing of the plume's arrival in Milan (as also seen from central Milan webcams, Fig. 12b) and show the vertical  
622 extent of the particle-rich layer associated with the episode. The plume continued to travel westward and was detected by the  
623 ALC in Aosta 4 hours later, indicating a wind speed  $> 12$  m/s. As revealed by both satellite measurements (Fig. 12c) and  
624 model simulations (Fig. 12d), this episode was due to an extended (about 100 km) gust front originating from the cold and  
625 intense Bora winds from East, resuspending and transporting soil-originated particles from the cultivated fields across the  
626 whole Po Valley.

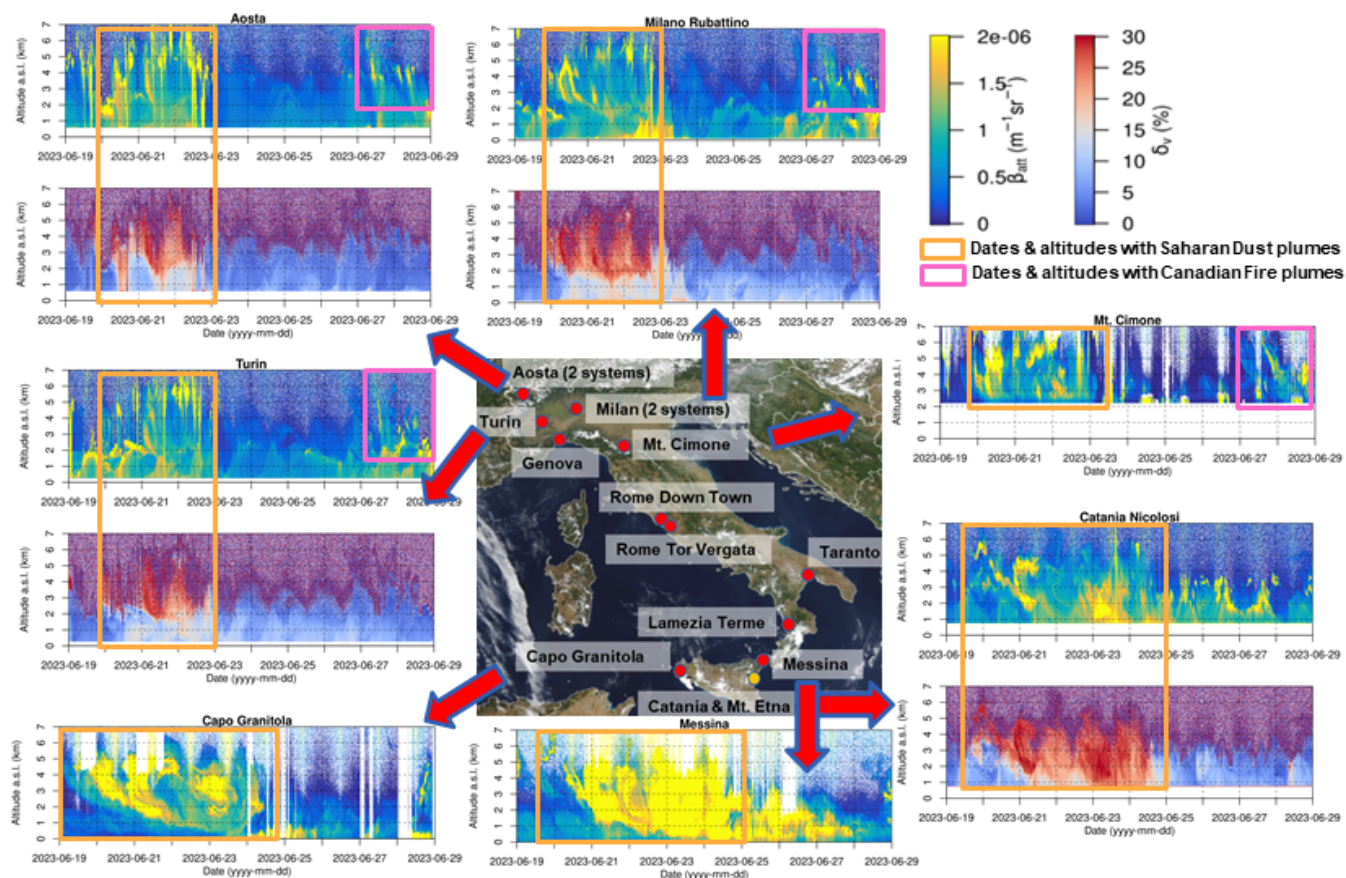
#### 627 **4.2 Advection of Saharan dust and Canadian fire plumes over Italy (19-28 June 2023)**

628 The Mediterranean area is frequently affected by the transport of desert dust from North Africa and the Middle East (e.g.,  
629 Barnaba and Gobbi, 2004; Querol et al., 2009; Basart et al., 2012a; Greilinger et al., 2019; Gama et al., 2020). In Italy, these  
630 events are estimated to reach the ground on 10% (Northern regions) to over 30% (Southern regions) of the days in a year,  
631 and to impact on surface daily-mean PM<sub>10</sub> concentrations with 10-15  $\mu\text{g}/\text{m}^3$  (Barnaba et al, 2022). The transport of fire  
632 plumes from global-to-medium distances is also an important contributor to surface PM concentrations. Concerning the  
633 global scale transport towards Europe, a significative contribution is given by forest fires regularly developing during boreal  
634 summers in Canada (e.g., Ceamanos et al., 2023; Shang et al., 2024), although a major contribution from agricultural fires in  
635 Europe has also been detected over the continent, particularly in spring and summer (Barnaba et al., 2011). Last summer  
636 (2023) was particularly impacted by multiple episodes of severe wildfires in central Canada. Almost 480 megatonnes of  
637 carbon were emitted, resulting in a major impact on AQ across Canada and the Northern US. The plumes have also been  
638 observed to be regularly transported towards Europe ([https://atmosphere.copernicus.eu/copernicus-canada-produced-23-  
639 global-wildfire-carbon-emissions-2023](https://atmosphere.copernicus.eu/copernicus-canada-produced-23-global-wildfire-carbon-emissions-2023), last access: 6-3-2024). Figure 13 shows a composite of measurements collected at  
640 multiple Alicenet sites across the country during a 10-days period (19-28 June 2023) affected by both desert-dust (time-  
641 range orange boxes) and forest-fire plumes (time-range magenta boxes). More specifically, this period was characterised by  
642 the intrusion of Saharan dust to Southern to Northern Italy (19-24 June 2023), followed by the transport of Canadian fire  
643 plumes over Central and Northern Italy (27-28 June 2023). The ALC profiles ( $\beta_{\text{att}}$  and  $\delta_v$ ) at the 7 selected Alicenet sites  
644 allow to follow the spatio-temporal evolution of the different aerosol layers and identify the relevant aerosol type. The  
645 Saharan dust layers were firstly observed over South-West Italy (Capo Granitola, June 19 in the morning), then moving  
646 westward to Messina and Catania Nicolosi (June 19, afternoon), and northward to Turin, Aosta, Milano, Mt. Cimone, where  
647 the dust plume is detected in the evening. All over Italy, the dust plume affects atmospheric layers up to 7 km altitude,  
648 reaching down to the surface on June 20. In fact, the PLC systems clearly indicate the presence of irregularly-shaped mineral



649 particles (depolarisation values > 30%), these mixing with local (mainly spherical) particles ( $\delta_v \sim 10\text{-}20\%$ ) when reaching the  
 650 lowermost levels.

651



652

653 **Figure 13:** Vertical profiles of total attenuated backscatter,  $\beta_{att}$  (ALCs & PLCs) and volume depolarisation,  $\delta_v$  (PLCs) for selected, North-  
 654 to-South Alicenet sites in the period 19-28 June 2023 affected by Saharan dust and Canadian fire plumes (orange and magenta boxes,  
 655 respectively). Central map: satellite true colour image (credits: EUMETSAT).

656

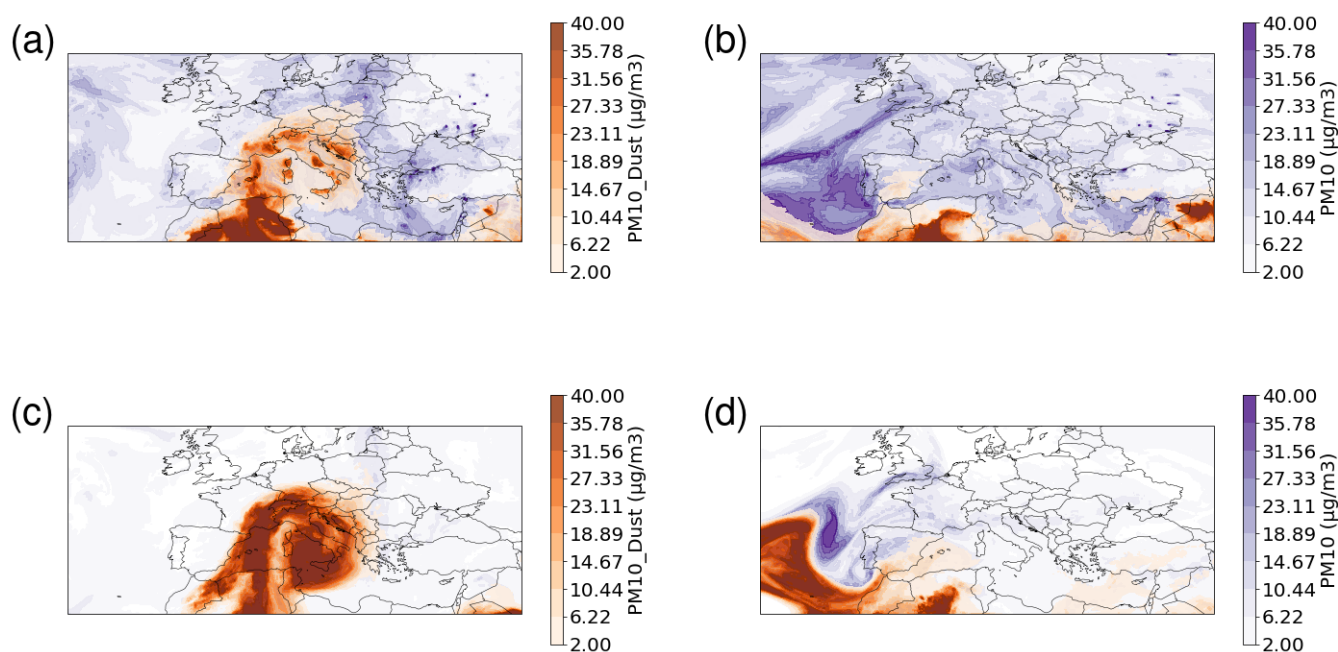
657 The Canadian fire plumes were firstly observed by Alicenet systems operating in Northern Italy on 27 June 2023, impacting  
 658 atmospheric levels in the range 2-7 km a.s.l. The plumes were firstly detected in Aosta, and then travelled through the whole  
 659 Po Valley, being clearly observed in Mt. Cimone. Being mainly composed of processed particles, these long-range  
 660 transported fire plumes do not show increases of depolarisation values, and appear as thinner aerosol layers with respect to  
 661 the ones typically associated with dust layers. These vertically resolved measurements well complement the information that  
 662 can be gathered from satellites as shown by this comparison of Alicenet data and MSG and Metop retrievals, limited to the  
 663 dust event (e.g., <https://vuser.eumetsat.int/resources/case-studies/dust-transport-from-the-sahara-to-the-mediterranean>, last  
 664 access: 6-3-2024). At the same time, this information also provides an observational verification of the picture that can be





665 obtained by modelling tools. In this respect, Fig. 14 shows the Ensemble CAMS EU forecast maps for two dates within the  
666 temporal window addressed: 22/06/2023 (dust intrusion, left panels) and 27/06/2023 (Canadian fires, bottom panels), at two  
667 altitude levels (100 and 3000 m a.g.l., top and bottom panels respectively). The horizontal evolution of the aerosol  
668 advectations qualitatively agrees with the information detected by Alicenet. It is more difficult to correctly model the aerosol  
669 vertical distribution, due to both their coarse vertical resolution and simplified parameterizations of the aerosol-related  
670 atmospheric processes (e.g., Koffi et al., 2016). Hence, remote sensing observations represent an added value, in particular  
671 for AQ monitoring, needing an accurate description of the timing and load of the aerosol injections in the lowermost  
672 atmospheric levels, and model validation exercises.

673



675 **Figure 14:** CAMS EU forecast of the total PM10 and PM10-dust component concentrations during the desert dust (22/06/2023 00:00 UTC  
676 - left panels) and the Canadian fires (27/06/2023 21:00 UTC - right panels) events of Figure 13, top (bottom) panels referring to 100 m  
677 (3000 m) altitude.

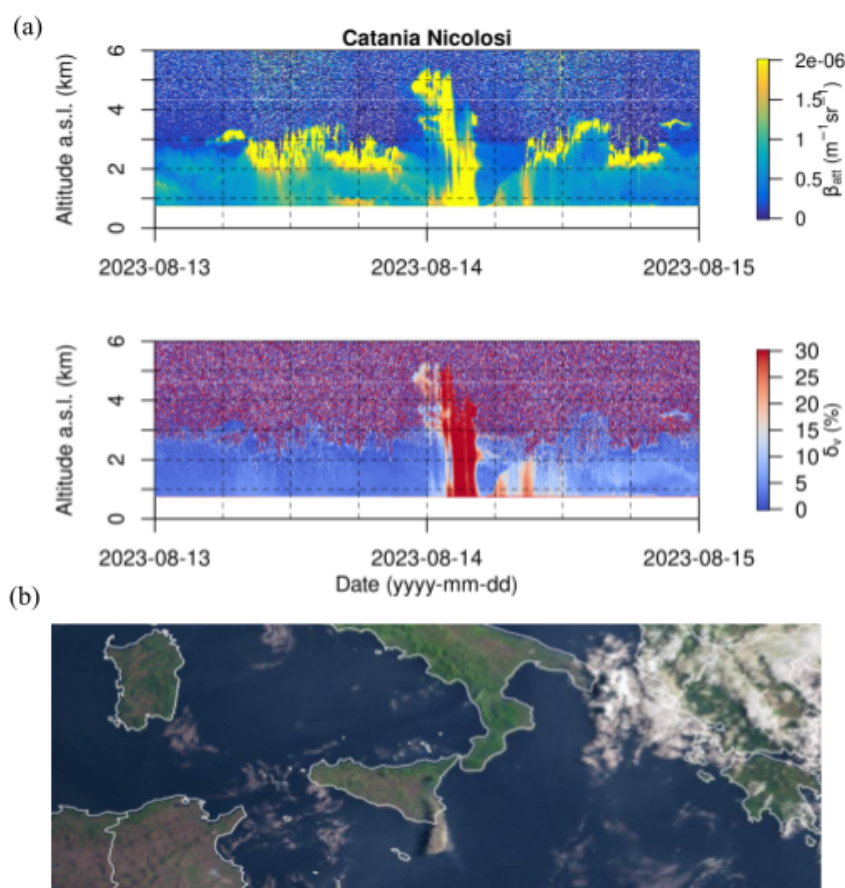
678

#### 679 4.3 Aerosol particles from the Mt. Etna eruption (13-14 August 2023)



680 A recent showcase from the Etna volcano eruption is reported here to highlight the important information that ALC/PLC  
681 observations can provide in volcanic areas to complement in situ, satellite-based and modelling data (e.g., Corradini et al.,  
682 2018, Scollo et al., 2019). During the night between 13 and 14 August 2023, this Europe's most active volcano erupted, its  
683 Southeast Crater emitting a volcanic cloud that the PLC in Catania Nicolosi detected to reach up to 5km at 21 UTC (Fig  
684 15a). On August 13, at 20:41 UTC, a Volcano Observatory Notice for Aviation (VONA) was issued by INGV  
685 ([https://www.ct.ingv.it/Dati/informative/vona/VONA\\_Etna\\_202308132041Z\\_2023005708E01.pdf](https://www.ct.ingv.it/Dati/informative/vona/VONA_Etna_202308132041Z_2023005708E01.pdf), last access: 06-03-2024)  
686 with a 'red alert' for aviation. VONA are short, plain-English messages aimed at dispatchers, pilots, and air-traffic  
687 controllers to inform them of volcanic unrest and eruptive activity that could produce ash-cloud hazards. In fact, flights  
688 serving Catania were halted. The most intense phase of the eruption occurred between 01:40-02:30 UTC, when PLC  
689 depolarisation values reached values > 40% indicating a predominance of irregular ash particles. The ash plume was then  
690 observed to rapidly reach down to the ground, while moving southward in the Mediterranean Sea (Fig 15b). In fact, less than  
691 5 hours after the beginning of the eruption the plume was detectable east of Malta. In agreement with the ALC record, the  
692 VONA issued by INGV at 05:54 UTC indicates that no ash plumes were produced and that the volcanic ash was confined in  
693 the summit areas of the volcano, this corresponding to an orange Aviation colour code  
694 ([https://www.ct.ingv.it/Dati/informative/vona/VONA\\_Etna\\_202308140554Z\\_2023005808F01.pdf](https://www.ct.ingv.it/Dati/informative/vona/VONA_Etna_202308140554Z_2023005808F01.pdf), last access: 06-03-2024).  
695





697 **Figure 15:** (a) Total attenuated backscatter,  $\beta_{att}$ , plus volume depolarisation,  $\delta_v$ , profiles observed at the Alicenet Catania Nicolosi site on  
698 13-14/08/2023; (b) METEOSAT Natural Colour Enhanced RGB (SEVIRI) image referring to 14/08/2023, 05:15 UTC (Credits:  
699 EUMETSAT).

700

## 701 5 Summary and future perspectives

702 In this work we present Alicenet, the Italian network of automated lidar-ceilometers (ALCs) operating from North to South  
703 across the peninsula. It is a cooperative network set up by CNR-ISAC in 2015, with active contributions from several  
704 national and regional institutions (e.g. regional EPAs, Universities, Research Centres and private companies). Some Alicenet  
705 ALCs also contribute to the European network E-PROFILE managed by EUMETNET to fill an Italian observational gap at  
706 the EU level. In fact, in most Member States meteorological agencies are typically responsible for ALC monitoring, some of  
707 these running over 100 instruments (e.g. the German meteorological service, DWD,

65  
66



708 [https://www.dwd.de/EN/research/observing\\_atmosphere/composition\\_atmosphere/aerosol/cont\\_nav/aerosolprofiles.html](https://www.dwd.de/EN/research/observing_atmosphere/composition_atmosphere/aerosol/cont_nav/aerosolprofiles.html),  
709 last access 7-3-2024).

710 In recent years the Alicenet network grew up and now includes about 20 active systems (Table 1) sampling in very different  
711 environments (urban, coastal, mountainous and volcanic areas), and thus providing information in a large spectrum of  
712 atmospheric conditions and aerosol types. Alicenet promoted a standardisation of instruments and an homogeneous data  
713 processing specifically developed within the network. It mainly runs single-channel ALCs (CHM15k systems by Lufft) but  
714 is progressively introducing polarisation-sensitive systems (PLCs) recently commercialised by Vaisala (CL61) to further  
715 exploit the ability of these systems to discriminate among aerosol types. Alicenet also intends to bridge a gap at the national  
716 level between the research-oriented and the operational use of active aerosol remote sensing devices in several sectors,  
717 among which: a) air quality, b) radiative budget/solar energy, c) validation of models and satellite products, d) aviation  
718 safety. In the first case, of particular interest are the abilities of the ALC/PLC-based Alicenet data to i) automatically identify  
719 medium-to-long range aerosol advections and estimate the relevant contribution to surface PM10 concentrations, and ii)  
720 provide continuous information on particulate matter layering, including the Mixing Aerosol Layer, i.e. on the atmospheric  
721 volume in which locally emitted particles are diluted (e.g., Kotthaus et al., 2023). The effectiveness of using these ALC/PLC  
722 abilities in support of standard air quality monitoring networks is being currently explored within the ongoing EU H2020  
723 Project RI-URBANS, aimed at developing an air quality monitoring system that complements those currently available. In  
724 this framework, tests of upscaling the Alicenet tools to other urban sites in the EU are in progress (Bellini et al., 2024b).  
725 Concerning the other applications mentioned above, the continuous ALC-based information on the aerosol loads and vertical  
726 distribution is useful to better estimate the relevant aerosol radiative effects (beneficial for example within an operational  
727 short-term solar forecasting system based on a multisensor approach, e.g. Papachristopoulou et al., 2024), for validation  
728 of/assimilation in models (e.g. Chan et al., 2018; Valmassoi et al., 2023), verification of satellite aerosol layering products  
729 (e.g., Janicke et al., 2023) including those foreseen from the upcoming EarthCare ESA mission (e.g., van Zadelhoff et al.,  
730 2023) or for the provision of near-real time alerts for aviation safety during specific extreme events such as desert dust  
731 storms and volcanic eruption (e.g., Papagiannopoulos et al., 2020).

732 Since the beginning of the Alicenet activities, particular care has been devoted to data retrievals and exploitation, this also  
733 taking advantage of technical/scientific exchanges within European initiatives, such as E-PROFILE and the EC Cost Actions  
734 TOPROF (2013-2016) and PROBE (2019-2024). To this purpose, Alicenet developed a specific, centralised and automated  
735 data processing chain and associated data quality assurance/data quality control (QA/QC) procedures which are presented in  
736 detail in this work. Overall, the data processing includes signal correction and calibration procedures (Sects. 3.1, 3.2) and  
737 retrieval algorithms for both quantitative aerosol properties (Sects. 3.3.1, 3.3.2) and aerosol layering (Sect. 3.4). The  
738 processing output thus includes basic-to-advanced aerosol products (L1-L3 products), ranging from attenuated backscatter  
739 and (if available) depolarisation profiles, to aerosol extinction and mass concentration profiles plus aerosol layering (e.g.,  
740 Mixed Aerosol Layer and Elevated Aerosol Layers). Vertical profiles of L1 and/or L2 products are provided in near real time  
741 on a dedicated website (<https://www.alice-net.eu/>, last access: 3 March 2024), while L3 products are routinely obtained



742 offline and are currently only available upon request. Examples of both product types are reported in Sect. 4 and Sect. 3,  
743 respectively. For L3 products, this work also includes direct comparisons with relevant, independent data (in-situ or remote  
744 sensing, depending on the variable addressed), this showing the Alicenet data processing to provide robust and quantitative  
745 aerosol information, within the discussed limits of the data accuracy (Sect. 3.3.3). In fact, long-term comparisons of aerosol  
746 mass retrievals with surface PM10 data show mean discrepancies of 35%, while AOD comparisons to thousands of relevant  
747 data points from co-located sun photometers show correlation coefficients  $> 0.8$  and fit slopes ranging between 0.8-1.0,  
748 depending on the site location.

749 A more extended analysis of the L3 products multi-annual datasets at different Alicenet sites located across Italy, , will be  
750 presented in a separate work (Bellini et al., 2024a), while an algorithm intercomparison exercise is currently in progress  
751 within PROBE to evaluate differences in the outcomes produced by different national networks in the EU (namely: Alicenet  
752 - Italy, MetOffice - UK, V-PROFILE - Norway, DWD - Germany).

753 Besides a geographical extension of the network (new stations are already planned to join in the next months), next steps  
754 foreseen for Alicenet, are: a) a better characterisation of the instruments artefacts and calibration, b) the extension of the  
755 Alicenet ALC retrieval methodology to different aerosol types, c) the development of a full retrieval for (CL61) PLCs,  
756 further exploiting the depolarisation information to complement aerosol layering with aerosol typing. The CL61 operating at  
757 a different wavelength with respect to CHM15k, this would require the evaluation of water vapour absorption corrections  
758 (e.g., Wiegner and Gasteiger, 2015), and the definition of new, wavelength specific functional relationships (e.g. Dionisi et  
759 al., 2018) to be used within the data inversion process. The feasibility of a routine dissemination of Alicenet L3 products via  
760 the network website in addition to the near-real time L1 and L2 ones is currently under evaluation.

761 Overall, Alicenet represents a valuable resource to complement the aerosol observational capabilities in Italy with the unique  
762 capacity of continuous 4D monitoring, thus bridging scientific research and operational applications. As for similar networks  
763 in Europe and beyond, maturity of both instrumental technologies and physics-based data processing tools as the ones  
764 described here suggest ALC/PLC networks could fruitfully contribute to aerosol measurements within the ACTRIS  
765 European Research Infrastructure, at the same time representing a good example of earth observation science applications  
766 for society.

767 **Code availability:** Codes used for data analysis can be provided upon request to the corresponding authors

768 **Data availability:** The presented datasets are made available to the Editor and Reviewers through a relevant shared directory  
769 (credential provided). These will be made freely accessible and linked to a doi, should the revision process lead to a positive  
770 outcome.

771 **Author Contribution:** Conceptualization, Data curation, Investigation: AnB, FB, HD; Formal analysis and Software: AnB;  
772 Visualization: AnB, FB, HD; ALC instruments and database management: LDL, AIB, FP, HD, GPG; Funding acquisition  
773 and Supervision: FB; Writing – original draft preparation: AnB, FB, HD; Writing – review & editing: AnB, FB, HD, AIB,  
774 GPG.



775 **Competing interests:** The authors declare that they have no conflict of interest.

## 776 **Acknowledgements**

777 This research received partial financial support from the EC H2020 Project RI-URBANS (GA No 101036245), and  
778 benefited from work done within the Action PROBE (CA18235), supported by COST (European Cooperation in Science and  
779 Technology).

780 A. Bellini performed this work in the framework of her Doctoral Program at University 'La Sapienza', DIET, Rome, Italy.

781 A. Bracci and F. Pasqualini were supported by the project IR0000032 – ITINERIS, Italian Integrated Environmental  
782 Research Infrastructures System, funded by EU - Next Generation EU, PNRR- Mission 4 “Education and Research” -  
783 Component 2: “From research to business” - Investment 3.1: “Fund for the realisation of an integrated system of research  
784 and innovation infrastructures”.

785 We would like to thank: M. Clerico and D. Poggi (PLC-Torino), R. Cresta and A. Bisignano (PLC-Genova), E. Collino and  
786 D. Perona (PLC-Milan-Rubattino), C. Cristofanelli (ALC-Mt.Cimone), S. Ottonelli (ALC-Taranto), C.R. Calidonna (ALC-  
787 Lamezia Terme), M. Coltelli and R. Gueli (Catania and Etna ALC & PLC systems) for their contribution to the Alicenet  
788 infrastructure, and L. Ferrero, A. Di Giosa, M. Furnari and G. Tranchida for support in the Alicenet sites of Milano Bicocca,  
789 Rome Downtown, Messina and Capo Granitola, respectively.

790 PLC data in Milan-Rubattino, are collected by RSE in the framework of the 3-Year Research Plan 2022-2024 for the Italian  
791 Electrical System (DM MITE n. 337, 15.09.2022), in compliance with the Decree of April 16th, 2018.

792 We acknowledge the Italian Air Force CAMM-Mt.Cimone for their support in the operation of the CMN-IT ceilometer,  
793 funded by the Ministry of University and Research (MUR) by the Project "Potenziamento della Rete di Osservazione ICOS-  
794 Italia nel Mediterraneo" PRO-ICOS\_MED (PIR01\_00019), and the GAW-WMO regional station "Rita Atria" for the  
795 ceilometer hosting in Capo Granitola.

796 We also gratefully acknowledge S. Gilardoni, P. Bonasoni and A. Provenzale for providing the OPC data collected at the  
797 'Testa Grigia' station at Plateau Rosa managed by the CNR Department of Earth System Sciences and Environmental  
798 Technologies, and the ARPA Lazio for providing the Rome Tor Vergata TKE dataset.

799 We acknowledge the Copernicus Atmosphere Monitoring Service (CAMS) for the CAMS European air quality forecasts,  
800 ENSEMBLE data: METEO FRANCE, Institut national de l'environnement industriel et des risques (Ineris), Aarhus  
801 University, Norwegian Meteorological Institute (MET Norway), Jülich Institut für Energie- und Klimaforschung (IEK),  
802 Institute of Environmental Protection – National Research Institute (IEP-NRI), Koninklijk Nederlands Meteorologisch  
803 Instituut (KNMI), Nederlandse Organisatie voor toegepast-natuurwetenschappelijk onderzoek (TNO), Swedish  
804 Meteorological and Hydrological Institute (SMHI), Finnish Meteorological Institute (FMI), Italian National Agency for New  
805 Technologies, Energy and Sustainable Economic Development (ENEA) and Barcelona Supercomputing Center (BSC)  
806 (2022): CAMS European air quality forecasts, ENSEMBLE data. Copernicus Atmosphere Monitoring Service (CAMS)  
807 Atmosphere Data Store (ADS), <https://atmosphere.copernicus.eu/>.



## 808 References

809 Adam, M., Fragkos, K., Biniotoglou, I., Wang, D., Stachlewska, I. S., Belegante, L., and Nicolae, V.: Towards Early  
810 Detection of Tropospheric Aerosol Layers Using Monitoring with Ceilometer, Photometer, and Air Mass Trajectories,  
811 Remote Sensing, 14(5):1217, <https://doi.org/10.3390/rs14051217>, 2022.

812

813 Andrés Hernández, M. D., Hilboll, A., Ziereis, H., Förster, E., Krüger, O. O., Kaiser, K., Schneider, J., Barnaba, F.,  
814 Vrekoussis, M., Schmidt, J., Huntrieser, H., Blechschmidt, A.-M., George, M., Nenakhov, V., Harlass, T., Holanda, B. A.,  
815 Wolf, J., Eirenschmalz, L., Krebsbach, M., Pöhlker, M. L., Kalisz Hedegaard, A. B., Mei, L., Pfeilsticker, K., Liu, Y.,  
816 Koppmann, R., Schlager, H., Bohn, B., Schumann, U., Richter, A., Schreiner, B., Sauer, D., Baumann, R., Mertens, M.,  
817 Jöckel, P., Kilian, M., Stratmann, G., Pöhlker, C., Campanelli, M., Pandolfi, M., Sicard, M., Gómez-Amo, J. L., Pujadas, M.,  
818 Bigge, K., Kluge, F., Schwarz, A., Daskalakis, N., Walter, D., Zahn, A., Pöschl, U., Bönisch, H., Borrmann, S., Platt, U., and  
819 Burrows, J. P.: Overview: On the transport and transformation of pollutants in the outflow of major population centres –  
820 observational data from the EMERGe European intensive operational period in summer 2017, Atmos. Chem. Phys., 22,  
821 5877–5924, <https://doi.org/10.5194/acp-22-5877-2022>, 2022.

822

823 Angelini, F., Barnaba, F., Landi, T. C., Caporaso, L., and Gobbi, G. P.: Study of atmospheric aerosols and mixing layer by  
824 LIDAR, Radiant. Prot. Dosim., 137, 275–279, <https://doi.org/10.1093/rpd/ncp219>, 2009.

825

826 Ansmann, A., Tesche, M., Seifert, P., Groß, S., Freudenthaler, V., Apituley, A., Wilson, K. M., Serikov, I., Linné, H.,  
827 Heinold, B., Hiebsch, A., Schnell, F., Schmidt, J., Mattis, I., Wandinger, U., and Wiegner, M.: Ash and fine-mode particle  
828 mass profiles from EARLINET-AERONET observations over central Europe after the eruptions of the Eyjafjallajökull  
829 volcano in 2010, J. Geophys. Res., 116, D00U02, doi:10.1029/2010JD015567, 2010.

830

831 Aubinet, M., Grelle, A., Ibrom, A., Rannik, Ü., Moncrieff, J., Foken T., Kowalski, A.S., Martin, P.H., Berbigier, P.,  
832 Bernhofer, Ch., Clement, R., Elbers, J., Granier, A., Grünwald, T., Morgenstern, K., Pilegaard, K., Rebmann, C., Snijders,  
833 W., Valentini, R., and Vesala, T.: Estimates of the Annual Net Carbon and Water Exchange of Forests: The EUROFLUX  
834 Methodology, Advances in Ecological Research, 30, 113-175, [https://doi.org/10.1016/S0065-2504\(08\)60018-5](https://doi.org/10.1016/S0065-2504(08)60018-5), 1999.

835

836 Balestrini, R., Diémoz, H., Freppaz, M., Delconte, C.A., Caschetto, M., Matiatos, I.: Nitrogen atmospheric deposition in a  
837 high-altitude Alpine environment: A chemical and isotopic approach to investigate the influence from anthropized areas,  
838 Atmos. Environ., 328, 120513, [doi: 10.1016/j.atmosenv.2024.120513](https://doi.org/10.1016/j.atmosenv.2024.120513), 2024.

839



840 Barnaba, F., and Gobbi, G. P.: Lidar estimation of tropospheric aerosol extinction, surface area and volume: Maritime and  
841 desert-dust cases, *J. Geophys. Res.*, 106(D3), 3005–3018, doi:10.1029/2000JD900492, 2001.

842

843 Barnaba, F., Putaud, J. P., Gruening, C., Dell’Acqua, A., and Dos Santos, S.: Annual cycle in co-located in situ, total-  
844 column,

845 and height-resolved aerosol observations in the Po Valley (Italy): Implications for ground-level particulate matter mass  
846 concentration estimation from remote sensing, *J. Geophys. Res.-Atmos.*, 115, D19209,  
847 <https://doi.org/10.1029/2009JD013002>, 2010.

848

849 Barnaba, F., Angelini, F., Curci, G., and Gobbi, G. P.: An important fingerprint of wildfires on the European aerosol load,  
850 *Atmos. Chem. Phys.*, 11, 10487–10501, <https://doi.org/10.5194/acp-11-10487-2011>, 2011.

851

852 Barnaba, F., Romero, N., Bolignano, A., Basart, S., Renzi, M., and Stafoggia, M.: Multiannual assessment of the desert dust  
853 impact on air quality in Italy combining PM10 data with physics-based and geostatistical models, *Environment International*,  
854 163, 107204, <https://doi.org/10.1016/j.envint.2022.107204>, 2022.

855

856 Bellini, A., Diémoz, H., Di Liberto, L., Gobbi G.P., Bracci, A., Pasqualini, F., and Barnaba, F.: Multi-annual analysis of  
857 aerosol vertical profiles and clouds across Italy derived from the Italian network of Automated Lidar-Ceilometers Alicenet,  
858 in preparation, 2024a.

859

860 Bellini, A., Diémoz, H., Di Liberto, L., Gobbi G.P., Bracci, A., Pasqualini, F., and Barnaba, F.: Quantitative analysis of  
861 aerosol profiles by automated lidar-ceilometers (ALC) in support of air quality monitoring in EU urban areas, in preparation,  
862 2024b.

863

864 Ceamanos, X., Coopman, Q., George, M., Riedi, J., Parrington, M., and Clerbaux, C.: Remote sensing and model analysis of  
865 biomass burning smoke transported across the Atlantic during the 2020 Western US wildfire season, *Sci. Rep.*, 13, 16014,  
866 <https://doi.org/10.1038/s41598-023-39312-1>, 2023.

867

868 Di Bernardino, A., Mazzarella, V., Pecci, M., Casasanta, G., Cacciani, M., and Ferretti, R.: Interaction of the Sea Breeze  
869 with the Urban Area of Rome: WRF Mesoscale and WRF Large-Eddy Simulations Compared to Ground-Based  
870 Observations, *Boundary-Layer Meteorol.*, 185, 333–363, <https://doi.org/10.1007/s10546-022-00734-5>, 2022.

871

872 Bonanno, R., Lacavalla, M., and Sperati, S.: A new high resolution Meteorological Reanalysis Italian Dataset: MERIDA, Q.  
873 *J. Roy. Meteorol. Soc.*, 145, 1756–1779, <https://doi.org/10.1002/qj.3530>, 2019.





874

875 Brenot, H., Theys, N., Clarisse, L., van Gent, J., Hurtmans, D. R., Vandenbussche, S., Papagiannopoulos, N., Mona, L.,  
876 Virtanen, T., Uppstu, A., Sofiev, M., Bugliaro, L., Vázquez-Navarro, M., Hedelt, P., Parks, M. M., Barsotti, S., Coltelli, M.,  
877 Moreland, W., Scollo, S., Salerno, G., Arnold-Arias, D., Hirtl, M., Peltonen, T., Lahtinen, J., Sievers, K., Lipok, F.,  
878 Rüfenacht, R., Haefele, A., Hervo, M., Wagenaar, S., Som de Cerff, W., de Laat, J., Apituley, A., Stammes, P., Laffineur,  
879 Q., Delcloo, A., Lennart, R., Rokitansky, C.-H., Vargas, A., Kerschbaum, M., Resch, C., Zopp, R., Plu, M., Peuch, V.-H.,  
880 Van Roozendaal, M., and Wotawa, G.: EUNADICS-AV early warning system dedicated to supporting aviation in the case of  
881 a crisis from natural airborne hazards and radionuclide clouds, *Nat. Hazards Earth Syst. Sci.*, 21, 3367–3405,  
882 <https://doi.org/10.5194/nhess-21-3367-2021>, 2021.

883

884 Breusch, T. S.: Testing for Autocorrelation in Dynamic Linear Models, *Australian Economic Papers*, 17, 334–355,  
885 doi:10.1111/j.1467-8454.1978.tb00635.x, 1978.

886

887 Bucci, S., Cristofanelli, P., Decesari, S., Marinoni, A., Sandrini, S., Größ, J., Wiedensohler, A., Di Marco, C. F., Nemitz, E.,  
888 Cairo, F., Di Liberto, L., and Fierli, F.: Vertical distribution of aerosol optical properties in the Po Valley during the 2012  
889 summer campaigns, *Atmos. Chem. Phys.*, 18, 5371–5389, <https://doi.org/10.5194/acp-18-5371-2018>, 2018.

890

891 Chan, K. L., Wiegner, M., Flentje, H., Mattis, I., Wagner, F., Gasteiger, J., and Geiß, A.: Evaluation of ECMWF-IFS  
892 (version 41R1) operational model forecasts of aerosol transport by using ceilometer network measurements, *Geosci. Model*  
893 *Dev.*, 11, 3807–3831, <https://doi.org/10.5194/gmd-11-3807-2018>, 2018.

894

895 Caicedo, V., Delgado, R., Sakai, R., Knepp, T., Williams, D., Cavender, K., Lefer, B., and Szykman, J.: An Automated  
896 Common Algorithm for Planetary Boundary Layer Retrievals Using Aerosol Lidars in Support of the U.S. EPA  
897 Photochemical Assessment Monitoring Stations Program, *J. Atmos. Oceanic Technol.*, 37, 1847–1864,  
898 <https://doi.org/10.1175/JTECH-D-20-0050.1>, 2020.

899

900 Collaud Coen, M., Weingartner, E., Furger, M., Nyeki, S., Prévôt, A. S. H., Steinbacher, M., and Baltensperger, U.: Aerosol  
901 climatology and planetary boundary influence at the Jungfraujoch analyzed by synoptic weather types, *Atmos. Chem. Phys.*,  
902 11, 5931–5944, <https://doi.org/10.5194/acp-11-5931-2011>, 2011.

903

904 Collaud Coen, M., Andrews, E., Aliaga, D., Andrade, M., Angelov, H., Bukowiecki, N., Ealo, M., Fialho, P., Flentje, H.,  
905 Hallar, A. G., Hooda, R., Kalapov, I., Krejci, R., Lin, N.-H., Marinoni, A., Ming, J., Nguyen, N. A., Pandolfi, M., Pont, V.,  
906 Ries, L., Rodríguez, S., Schauer, G., Sellegri, K., Sharma, S., Sun, J., Tunved, P., Velasquez, P., and Ruffieux, D.:





907 Identification of topographic features influencing aerosol observations at high altitude stations, *Atmos. Chem. Phys.*, 18,  
908 12289–12313, <https://doi.org/10.5194/acp-18-12289-2018>, 2018.

909

910 Córdoba-Jabonero, C., Sicard, M., Ansmann, A., del Águila, A., and Baars, H.: Separation of the optical and mass features  
911 of particle components in different aerosol mixtures by using POLIPHON retrievals in synergy with continuous polarized  
912 Micro-Pulse Lidar (P-MPL) measurements, *Atmos. Meas. Tech.*, 11, 4775–4795, <https://doi.org/10.5194/amt-11-4775-2018>,  
913 2018.

914

915 Corradini, S., Guerrieri, L., Lombardo, V., Merucci, L., Musacchio, M., Prestifilippo, M., Scollo, S., Silvestri, M., Spata, G.,  
916 and Stelitano, D.: Proximal monitoring of the 2011-2015 Etna lava fountains using MSG-SEVIRI data. *Geosciences*, 8, 140,  
917 <https://doi.org/10.3390/geosciences8040140>, 2018.

918

919 Curci, G., Ferrero, L., Tuccella, P., Barnaba, F., Angelini, F., Bolzacchini, E., Carbone, C., Denier van der Gon, H. A. C.,  
920 Facchini, M. C., Gobbi, G. P., Kuenen, J. P. P., Landi, T. C., Perrino, C., Perrone, M. G., Sangiorgi, G., and Stocchi, P.: How  
921 much is particulate matter near the ground influenced by upper-level processes within and above the PBL? A summertime  
922 case study in Milan (Italy) evidences the distinctive role of nitrate, *Atmos. Chem. Phys.*, 15, 2629–2649,  
923 <https://doi.org/10.5194/acp-15-2629-2015>, 2015.

924

925 D'Angelo, L., Rovelli, G., Casati, M., Sangiorgi, G., Perrone, M. G., Bolzacchini, E., and Ferrero, L.: Seasonal behaviour of  
926 PM<sub>2.5</sub> deliquescence, crystallization, and hygroscopic growth in the Po Valley (Milan): Implications for remote sensing  
927 applications, *Atmospheric Research*, 176–177, 87-95, <https://doi.org/10.1016/j.atmosres.2016.02.011>, 2016.

928

929 Diémoz, H., Magri, T., Pession, G., Tarricone, C., Tombolato, I.K.F., Fasano, G., and Zublena, M.: Air Quality in the Italian  
930 Northwestern Alps during Year 2020: Assessment of the COVID-19 «Lockdown Effect» from Multi-Technique  
931 Observations and Models, *Atmosphere*, 12(8):1006, <https://doi.org/10.3390/atmos12081006>, 2021.

932

933 Diémoz, H., Barnaba, F., Magri, T., Pession, G., Dionisi, D., Pittavino, S., Tombolato, I. K. F., Campanelli, M., Della Ceca,  
934 L. S., Hervo, M., Di Liberto, L., Ferrero, L., and Gobbi, G. P.: Transport of Po Valley aerosol pollution to the northwestern  
935 Alps – Part 1: Phenomenology, *Atmos. Chem. Phys.*, 19, 3065–3095, <https://doi.org/10.5194/acp-19-3065-2019>, 2019.

936

937 Diémoz, H., Gobbi, G. P., Magri, T., Pession, G., Pittavino, S., Tombolato, I. K. F., Campanelli, M., and Barnaba, F.:  
938 Transport of Po Valley aerosol pollution to the northwestern Alps – Part 2: Long-term impact on air quality, *Atmos. Chem.*  
939 *Phys.*, 19, 10129–10160, <https://doi.org/10.5194/acp-19-10129-2019>, 2019.

940



941 Dionisi, D., Barnaba, F., Diémoz, H., Di Liberto, L., and Gobbi, G. P.: A multiwavelength numerical model in support of  
942 quantitative retrievals of aerosol properties from automated lidar ceilometers and test applications for AOT and PM10  
943 estimation, *Atmos. Meas. Tech.*, 11, 6013–6042, <https://doi.org/10.5194/amt-11-6013-2018>, 2018.

944

945 Du, P., Kibbe, W. A., and Lin, S. M.: Improved peak detection in mass spectrum by incorporating continuous wavelet  
946 transform-based pattern matching, *Bioinformatics*, 22:17, 2059–2065, <https://doi.org/10.1093/bioinformatics/btl355>, 2006.

947

948 Fasano, G., Diémoz, H., Fountoulakis, I., Cassardo, C., Kudo, R., Siani, A. M., and Ferrero, L.: Vertical profile of the clear-  
949 sky aerosol direct radiative effect in an Alpine valley, by the synergy of ground-based measurements and radiative transfer  
950 simulations, *Bull. of Atmos. Sci. & Technol.*, 2, 11, <https://doi.org/10.1007/s42865-021-00041-w>, 2021.

951

952 Ferrero, L., Riccio, A., Ferrini, B.S., D'Angelo, L., Rovelli, G., Casati, M., Angelini, F., Barnaba, F., Gobbi, G.P., Cataldi,  
953 M., Bolzacchini, E.: Satellite AOD conversion into ground PM10, PM2.5 and PM1 over the Po valley (Milan, Italy)  
954 exploiting information on aerosol vertical profiles, chemistry, hygroscopicity and meteorology, *Atmospheric Pollution*  
955 *Research*, 10:6, 1895-1912, <https://doi.org/10.1016/j.apr.2019.08.003>, 2019.

956

957 Flentje, H., Claude, H., Elste, T., Gilge, S., Köhler, U., Plass-Dülmer, C., Steinbrecht, W., Thomas, W., Werner, A., and  
958 Fricke, W.: The Eyjafjallajökull eruption in April 2010 – detection of volcanic plume using in-situ measurements, ozone  
959 sondes and lidar-ceilometer profiles, *Atmos. Chem. Phys.*, 10, 10085–10092, <https://doi.org/10.5194/acp-10-10085-2010>,  
960 2010.

961

962 Flentje, H., Mattis, I., Kipling, Z., Rémy, S., and Thomas, W.: Evaluation of ECMWF IFS-AER (CAM5) operational  
963 forecasts during cycle 41r1–46r1 with calibrated ceilometer profiles over Germany, *Geosci. Model Dev.*, 14, 1721–1751,  
964 <https://doi.org/10.5194/gmd-14-1721-2021>, 2021.

965

966 Fountoulakis, I., Papachristopoulou, K., Proestakis, E., Amiridis, V., Kontoes, C., and Kazadzis, S.: Effect of Aerosol  
967 Vertical Distribution on the Modeling of Solar Radiation, *Remote Sensing*, 14(5):1143, <https://doi.org/10.3390/rs14051143>,  
968 2022.

969

970 Giovannini, L., Ferrero, E., Karl, T., Rotach, M. W., Staquet, C., Trini Castelli, S., and Zardi, D.: Atmospheric Pollutant  
971 Dispersion over Complex Terrain: Challenges and Needs for Improving Air Quality Measurements and Modeling,  
972 *Atmosphere*, 11(6):646, <https://doi.org/10.3390/atmos11060646>, 2020.

973



- 974 Gobbi, G.P., Barnaba, F., Di Liberto, L., Bolignano, A., Lucarelli, F., Nava, S., Perrino, C., Pietrodangelo, A., Basart, S.,  
975 Costabile, F., Dionisi, D., Rizza, U., Canepari, S., Sozzi, R., Morelli, M., Manigrasso, M., Drewnick, F., Struckmeier, C.,  
976 Poenitz, K., and Wille, H.: An inclusive view of Saharan dust advections to Italy and the Central Mediterranean,  
977 *Atmospheric Environment*, 201, 242-256, <https://doi.org/10.1016/j.atmosenv.2019.01.002>, 2019.
- 978
- 979 Gobb, G.P., Barnaba, F., Blumthaler, M., Labow, G., and Herman, J.R.: Observed effects of particles nonsphericity on the  
980 retrieval of marine and desert dust aerosol optical depth by lidar, *Atmospheric Research*, 61:1, 1-14,  
981 [https://doi.org/10.1016/S0169-8095\(01\)00104-1](https://doi.org/10.1016/S0169-8095(01)00104-1), 2002.
- 982
- 983 Giorgino, T.: Computing and Visualizing Dynamic Time Warping Alignments in R: The dtw Package. *Journal of Statistical*  
984 *Software*, 31(7), 1–24, <https://doi.org/10.18637/jss.v031.i07>, 2009.
- 985
- 986 Haeffelin, M., Angelini, F., Morille, Y., Martucci, G., Frey, S., Gobbi, G. P., Lolli, S., O’Dowd, C. D., Sauvage, L., Xueref-  
987 Rémy, I., Wastine, B., and Feist D. G.: Evaluation of Mixing-Height Retrievals from Automatic Profiling Lidars and  
988 Ceilometers in View of Future Integrated Networks in Europe, *Boundary-Layer Meteorol.*, 143, 49–75,  
989 <https://doi.org/10.1007/s10546-011-9643-z>, 2012.
- 990
- 991 Haeffelin, M., Laffineur, Q., Bravo-Aranda, J.-A., Drouin, M.-A., Casquero-Vera, J.-A., Dupont, J.-C., and De Backer, H.:  
992 Radiation fog formation alerts using attenuated backscatter power from automatic lidars and ceilometers, *Atmos. Meas.*  
993 *Tech.*, 9, 5347–5365, <https://doi.org/10.5194/amt-9-5347-2016>, 2016.
- 994
- 995 Hervo, M., Poltera, Y., and Haefele, A.: An empirical method to correct for temperature-dependent variations in the overlap  
996 function of CHM15k ceilometers, *Atmos. Meas. Tech.*, 9, 2947–2959, <https://doi.org/10.5194/amt-9-2947-2016>, 2016.
- 997
- 998 Illingworth, A.J., Barker, H.W., Beljaars, A., Ceccaldi, M., Chepfer, H., Clerbaux, N., Cole, J., Delanoë, J., Domenech, C.,  
999 Donovan, D.P., Fukuda, S., Hirakata, M., Hogan, R. J., Huenerbein, A., Kollias, P., Kubota T., Nakajima, T., Nakajima, T.,  
1000 Y., Nishizawa, T., Ohno, Y., Okamoto, H., Oki, R., Sato, K., Satoh, M., Shephard, M. W., Velázquez-Blázquez, A.,  
1001 Wandinger, U., Wehr, T., and van Zadelhoff, G. J.: The EarthCARE satellite: The next step forward in global measurements  
1002 of clouds, aerosols, precipitation, and radiation. *Bull. Am. Meteorol. Soc.*, 96, 1311–1332, 10.1175/BAMS-D-12-00227.1,  
1003 2015.
- 1004
- 1005 Jänicke, L.K., Preusker, R., Docter, N., Fischer, J.: Estimation of Aerosol Layer Height from OLCI Measurements in the  
1006 O2A-Absorption Band over Oceans, *Remote Sensing*, 15(16):4080. <https://doi.org/10.3390/rs15164080>, 2023.
- 1007



1008 IPCC, 2022: Climate Change 2022: Impacts, Adaptation, and Vulnerability. Contribution of Working Group II to the Sixth  
1009 Assessment Report of the Intergovernmental Panel on Climate Change, Cambridge University Press, 3056,  
1010 doi:10.1017/9781009325844, 2022.

1011

1012 Kotthaus, S., Haeffelin, M., Drouin, M.-A., Dupont, J.-C., Grimmond, S., Haeferle, A., Hervo, M., Poltera, Y., Wiegner, M.:  
1013 Tailored Algorithms for the Detection of the Atmospheric Boundary Layer Height from Common Automatic Lidars and  
1014 Ceilometers (ALC), *Remote Sensing*, 12(19):3259, <https://doi.org/10.3390/rs12193259>, 2020.

1015

1016 Kotthaus, S., Bravo-Aranda, J. A., Collaud Coen, M., Guerrero-Rascado, J. L., Costa, M. J., Cimini, D., O'Connor, E. J.,  
1017 Hervo, M., Alados-Arboledas, L., Jiménez-Portaz, M., Mona, L., Ruffieux, D., Illingworth, A., and Haeffelin, M.:  
1018 Atmospheric boundary layer height from ground-based remote sensing: a review of capabilities and limitations, *Atmos.*  
1019 *Meas. Tech.*, 16, 433–479, <https://doi.org/10.5194/amt-16-433-2023>, 2023.

1020

1021 Klett J. D.: Lidar inversion with variable backscatter/extinction ratios, *Appl. Opt.* 24, 1638-1643,  
1022 <https://doi.org/10.1364/AO.24.001638>, 1985.

1023

1024 Michalsky, J.: The Astronomical Almanac's algorithm for approximate solar position (1950–2050), *Solar Energy*, 40(3),  
1025 227-235, [https://doi.org/10.1016/0038-092X\(88\)90045-X](https://doi.org/10.1016/0038-092X(88)90045-X), 1988.

1026

1027 Monteiro, A., Basart, S., Kazadzis, S., Votsis, A., Gkikas, A., Vandenbussche, S., Tobias, A., Gama, C., Pérez García-Pando,  
1028 C., Terradellas, E., Notas, G., Middleton, K., Kushta, J., Amiridis, V., Lagouvardos, K., Kosmopoulos, P., Kotroni, V.,  
1029 Kanakidou, M., Mihalopoulos, N., Kalivitis, N., Dagsson-Waldhauserová, P., El-Askary, H., Sievers, K., Giannaros, T.,  
1030 Mona, L., Hirtl, M., Skomorowski, P., Virtanen, T., Christoudias, T., Di Mauro, B., Trippetta, S., Kutuzov, S., Meinander,  
1031 O., and Nickovic, S.: Multi-sectoral impact assessment of an extreme African dust episode in the Eastern Mediterranean in  
1032 March 2018, *Science of The Total Environment*, 843, <https://doi.org/10.1016/j.scitotenv.2022.156861>, 2022.

1033

1034 Morille, Y., Haeffelin, M., Drobinski, P., and Pelon J.: STRAT: An Automated Algorithm to Retrieve the Vertical Structure  
1035 of the Atmosphere from Single-Channel Lidar Data, *J. Atmos. Oceanic Technol.*, 24, 761–775,  
1036 <https://doi.org/10.1175/JTECH2008.1>, 2007.

1037

1038 Mortier, A., Goloub, P., Podvin, T., Deroo, C., Chaikovsky, A., Ajtai, N., Blarel, L., Tanre, D., and Derimian, Y.: Detection  
1039 and characterization of volcanic ash plumes over Lille during the Eyjafjallajökull eruption, *Atmos. Chem. Phys.*, 13, 3705–  
1040 3720, <https://doi.org/10.5194/acp-13-3705-2013>, 2013.

1041



- 1042 Napoli, A., Desbiolles, F., Parodi, A., and Pasquero, C.: Aerosol indirect effects in complex-orography areas: a numerical  
1043 study over the Great Alpine Region, *Atmos. Chem. Phys.*, 22, 3901–3909, <https://doi.org/10.5194/acp-22-3901-2022>, 2022.  
1044
- 1045 Nicolae, D., Vasilescu, J., Talianu, C., Binietoglou, I., Nicolae, V., Andrei, S., and Antonescu, B.: A neural network aerosol-  
1046 typing algorithm based on lidar data, *Atmos. Chem. Phys.*, 18, 14511–14537, <https://doi.org/10.5194/acp-18-14511-2018>,  
1047 2018.  
1048
- 1049 Omar, A. H., Winker D. M., Vaughan, M. A., Hu, Y., Treppe, C. R., Ferrare, R. A., Lee K. P., Hostetler, C., Kittaka, C.,  
1050 Rogers, R. R., Kuehn R. E., and Liu, Z.: The CALIPSO Automated Aerosol Classification and Lidar Ratio Selection  
1051 Algorithm, *J. Atmos. Oceanic Technol.*, 26, 1994–2014, <https://doi.org/10.1175/2009JTECHA1231.1>, 2009.  
1052
- 1053 Osborne, M. J., de Leeuw, J., Witham, C., Schmidt, A., Beckett, F., Kristiansen, N., Buxmann, J., Saint, C., Welton, E. J.,  
1054 Fochesatto, J., Gomes, A. R., Bundke, U., Petzold, A., Marengo, F., and Haywood, J.: The 2019 Raikoke volcanic eruption –  
1055 Part 2: Particle-phase dispersion and concurrent wildfire smoke emissions, *Atmos. Chem. Phys.*, 22, 2975–2997,  
1056 <https://doi.org/10.5194/acp-22-2975-2022>, 2022.  
1057
- 1058 Papachristopoulou, K., Fountoulakis, I., Bais, A. F., Psiloglou, B. E., Papadimitriou, N., Raptis, I.-P., Kazantzidis, A.,  
1059 Kontoes, C., Hatzaki, M., and Kazadzis, S.: Effects of clouds and aerosols on downwelling surface solar irradiance  
1060 nowcasting and short-term forecasting, *Atmos. Meas. Tech. Discuss.*, <https://doi.org/10.5194/amt-2023-110>, accepted for  
1061 publication 2024.  
1062
- 1063 Papagiannopoulos, N., D'Amico, G., Gialitaki, A., Ajtai, N., Alados-Arboledas, L., Amodeo, A., Amiridis, V., Baars, H.,  
1064 Balis, D., Binietoglou, I., Comerón, A., Dionisi, D., Falconieri, A., Fréville, P., Kampouri, A., Mattis, I., Mijić, Z., Molero,  
1065 F., Papayannis, A., Pappalardo, G., Rodríguez-Gómez, A., Solomos, S., and Mona, L.: An EARLINET early warning system  
1066 for atmospheric aerosol aviation hazards, *Atmos. Chem. Phys.*, 20, 10775–10789, [https://doi.org/10.5194/acp-20-10775-](https://doi.org/10.5194/acp-20-10775-2020)  
1067 2020, 2020.  
1068
- 1069 Poltera, Y., Martucci, G., Collaud Coen, M., Hervo, M., Emmenegger, L., Henne, S., Brunner, D., and Haeefe, A.:  
1070 PathfinderTURB: an automatic boundary layer algorithm. Development, validation and application to study the impact on in  
1071 situ measurements at the Jungfraujoch, *Atmos. Chem. Phys.*, 17, 10051–10070, <https://doi.org/10.5194/acp-17-10051-2017>,  
1072 2017.  
1073
- 1074 Remer, L. A., Levy, R. C., and Martins, J. V.: Opinion: Aerosol remote sensing over the next 20 years, *Atmos. Chem. Phys.*,  
1075 24, 2113–2127, <https://doi.org/10.5194/acp-24-2113-2024>, 2024.



- 1076
- 1077 Rizza, U., Avolio, E., Morichetti, M., Di Liberto, L., Bellini, A., Barnaba, F., Virgili, S., Passerini, G., and Mancinelli, E.:
- 1078 On the Interplay between Desert Dust and Meteorology Based on WRF-Chem Simulations and Remote Sensing
- 1079 Observations in the Mediterranean Basin, *Remote Sensing*, 15(2):435, <https://doi.org/10.3390/rs15020435>, 2023.
- 1080
- 1081 Rodríguez, S., Querol, X., Alastuey, A., Kallos, G, and Kakaliagou, O.: Saharan dust contributions to PM<sub>10</sub> and TSP levels
- 1082 in Southern and Eastern Spain, *Atmospheric Environment*, 35(24), 33-2447, [https://doi.org/10.1016/S1352-2310\(00\)00496-](https://doi.org/10.1016/S1352-2310(00)00496-9)
- 1083 [9](https://doi.org/10.1016/S1352-2310(00)00496-9), 2001.
- 1084
- 1085 Sandrini, S., van Pinxteren, D., Giulianelli, L., Herrmann, H., Poulain, L., Facchini, M. C., Gilardoni, S., Rinaldi, M.,
- 1086 Paglione, M., Turpin, B. J., Pollini, F., Bucci, S., Zanca, N., and Decesari, S.: Size-resolved aerosol composition at an urban
- 1087 and a rural site in the Po Valley in summertime: implications for secondary aerosol formation, *Atmos. Chem. Phys.*, 16,
- 1088 10879–10897, <https://doi.org/10.5194/acp-16-10879-2016>, 2016.
- 1089
- 1090 Scollo, S., Prestifilippo, M., Bonadonna, C., Cioni, R., Corradini, S., Degruyter, W., Rossi, E., Silvestri, M., Biale, E.,
- 1091 Carparelli, G., Cassisi, C., Merucci, L., Musacchio, M., and Pecora, E.: Near-Real-Time Tephra Fallout Assessment at Mt.
- 1092 Etna, Italy, *Remote Sensing*, 11(24):2987, <https://doi.org/10.3390/rs11242987>, 2019.
- 1093
- 1094 Serafin, S., Adler, B., Cuxart, J., De Wekker, S.F.J., Gohm, A., Grisogono, B., Kalthoff, N., Kirshbaum, D.J., Rotach, M.W.,
- 1095 Schmidli, J., Stiperski, I., Večenaj, Z., and Zardi, D.: Exchange Processes in the Atmospheric Boundary Layer Over
- 1096 Mountainous Terrain. *Atmosphere*. 2018; 9(3):102. <https://doi.org/10.3390/atmos9030102>, 2018.
- 1097
- 1098 Shang, X., Lipponen, A., Filioglou, M., Sundström, A.-M., Parrington, M., Buchard, V., Darmenov, A. S., Welton, E. J.,
- 1099 Marinou, E., Amiridis, V., Sicard, M., Rodríguez-Gómez, A., Komppula, M., and Mielonen, T.: Monitoring biomass burning
- 1100 aerosol transport using CALIOP observations and reanalysis models: a Canadian wildfire event in 2019, *Atmos. Chem.*
- 1101 *Phys.*, 24, 1329–1344, <https://doi.org/10.5194/acp-24-1329-2024>, 2024.
- 1102
- 1103 Shang, X., Mielonen, T., Lipponen, A., Giannakaki, E., Leskinen, A., Buchard, V., Darmenov, A. S., Kukkurainen, A.,
- 1104 Arola, A., O'Connor, E., Hirsikko, A., and Komppula, M.: Mass concentration estimates of long-range-transported Canadian
- 1105 biomass burning aerosols from a multi-wavelength Raman polarisation lidar and a ceilometer in Finland, *Atmos. Meas.*
- 1106 *Tech.*, 14, 6159–6179, <https://doi.org/10.5194/amt-14-6159-2021>, 2021.
- 1107



- 1108 Shimizu, A., Nishizawa, T., Jin, Y., Kim, S.-W., Wang, Z., Batdorj, D., and Sugimoto, N.: Evolution of a lidar network for  
1109 tropospheric aerosol detection in East Asia, SPIE. Optical Engineering, 56, 1–12, <https://doi.org/10.1117/1.OE.56.3.031219>,  
1110 2016.
- 1111
- 1112 Speidel, J. and Vogelmann, H.: Correct(ed) Klett–Fernald algorithm for elastic aerosol backscatter retrievals: a sensitivity  
1113 analysis, Appl. Opt. 62, 861–868, <https://doi.org/10.1364/AO.465944>, 2023.
- 1114
- 1115 Tesche, M., Ansmann, A., Müller, D., Althausen, D., Engelmann, R., Freudenthaler, V., and Groß, S.: Vertically resolved  
1116 separation of dust and smoke over Cape Verde using multiwavelength Raman and polarisation lidars during Saharan Mineral  
1117 Dust Experiment 2008, J. Geophys. Res., 114, D13202, doi:10.1029/2009JD011862, 2009.
- 1118
- 1119 Tositti, L., Brattich, E., Cassardo, C., Morozzi, P., Bracci, A., Marinoni, A., Di Sabatino, S., Porcù, F., and Zappi, A.:  
1120 Development and evolution of an anomalous Asian dust event across Europe in March 2020, Atmos. Chem. Phys., 22, 4047–  
1121 4073, <https://doi.org/10.5194/acp-22-4047-2022>, 2022.
- 1122
- 1123 Uchiyama, A., Matsunaga, T., and Yamazaki, A.: The instrument constant of sky radiometers (POM-02) – Part 2: Solid view  
1124 angle, Atmos. Meas. Tech., 11, 5389–5402, <https://doi.org/10.5194/amt-11-5389-2018>, 2018.
- 1125
- 1126 Van Tricht, K., Gorodetskaya, I. V., Lhermitte, S., Turner, D. D., Schween, J. H., and Van Lipzig, N. P. M.: An improved  
1127 algorithm for polar cloud-base detection by ceilometer over the ice sheets, Atmos. Meas. Tech., 7, 1153–1167,  
1128 <https://doi.org/10.5194/amt-7-1153-2014>, 2014.
- 1129
- 1130 van Zadelhoff, G.-J., Donovan, D. P., and Wang, P.: Detection of aerosol and cloud features for the EarthCARE atmospheric  
1131 lidar (ATLID): the ATLID FeatureMask (A-FM) product, Atmos. Meas. Tech., 16, 3631–3651, <https://doi.org/10.5194/amt-16-3631-2023>, 2023.
- 1132
- 1133
- 1134 Vivone, G., D'Amico, G., Summa, D., Lolli, S., Amodeo, A., Bortoli, D., and Pappalardo, G.: Atmospheric boundary layer  
1135 height estimation from aerosol lidar: a new approach based on morphological image processing techniques, Atmos. Chem.  
1136 Phys., 21, 4249–4265, <https://doi.org/10.5194/acp-21-4249-2021>, 2021
- 1137
- 1138 Wiegner, M. and Gasteiger, J.: Correction of water vapour absorption for aerosol remote sensing with ceilometers, Atmos.  
1139 Meas. Tech., 8, 3971–3984, <https://doi.org/10.5194/amt-8-3971-2015>, 2015.
- 1140





- 1141 Wiegner, M., Madonna, F., Biniotoglou, I., Forkel, R., Gasteiger, J., Geiß, A., Pappalardo, G., Schäfer, K., and Thomas, W.:  
1142 What is the benefit of ceilometers for aerosol remote sensing? An answer from EARLINET, *Atmos. Meas. Tech.*, 7, 1979–  
1143 1997, <https://doi.org/10.5194/amt-7-1979-2014>, 2014.
- 1144
- 1145 Winker, D.M., Pelon, J., Coakley, J.A., Ackerman, S.A., Charlson, R.J., Colarco, P.R., Flamant, P., Fu, Q., Hoff, R.M.,  
1146 Kittaka, C., : The CALIPSO mission: A global 3D view of aerosols and clouds. *Bull. Am. Meteorol. Soc.*, 91, 1211–1230,  
1147 <https://doi.org/10.1175/2010BAMS3009.1>, 2010.
- 1148
- 1149 Welton, E.J., Campbell, J. R., Spinhirne, J. D., and Scott, V. S.: Global monitoring of clouds and aerosols using a network of  
1150 micro-pulse lidar systems, *Proc. SPIE*, 4153, 151-158, 10.1117/12.417040, 2000.
- 1151
- 1152 Welton, E. J., Stewart, S. A., Lewis, J. R., Belcher, L. R., Campbell, J. R., and Lolli, S.: Status of the NASA Micro Pulse  
1153 Lidar Network (MPLNET): overview of the network and future plans, new version 3 data products, and the polarised MPL,  
1154 *EPJ Web Conf.*, 176, 09003, <https://doi.org/10.1051/EPJCONF/201817609003>, 2018.
- 1155
- 1156 WHO, 2021: WHO global air quality guidelines: particulate matter (PM<sub>2.5</sub> and PM<sub>10</sub>), ozone, nitrogen dioxide, sulphur  
1157 dioxide and carbon monoxide, Licence: CC BY-NC-SA 3.0 IGO, <https://iris.who.int/handle/10665/345329> , 2021.